JGR Atmospheres

RESEARCH ARTICLE
10.1029/2023JD039572

Aitken Mode Aerosols Buffer Decoupled Mid-Latitude Boundary Layer Clouds Against Precipitation Depletion

Isabel L. McCoy[1,2,3,4], Matthew C. Wyant[1], Peter N. Blossey[1], Christopher S. Bretherton[5], and Robert Wood[1]

[1]Department of Atmospheric Sciences, University of Washington, Seattle, WA, USA, [2]Cooperative Programs for the Advancement of Earth System Science, University Corporation for Atmospheric Research, Boulder, CO, USA, [3]Cooperative Institute for Research in Environmental Sciences, University of Colorado, Boulder, CO, USA, [4]Chemical Sciences Laboratory, National Oceanic and Atmospheric Administration, Boulder, CO, USA, [5]Allen Institute for Artificial Intelligence, Seattle, WA, USA

Key Points:

- Observations of mid-latitude decoupled low clouds constrain a large-eddy simulation investigating aerosol-cloud-precipitation interactions
- Boundary layer Aitken activation and turbulent and convective fluxes restore accumulation mode aerosols against precipitation losses
- Aitken buffering acts to sustain brighter, more homogeneous clouds for longer

Supporting Information:

Supporting Information may be found in the online version of this article.

Correspondence to:

I. L. McCoy,
isabel.mccoy@noaa.gov

Citation:

McCoy, I. L., Wyant, M. C., Blossey, P. N., Bretherton, C. S., & Wood, R. (2024). Aitken mode aerosols buffer decoupled mid-latitude boundary layer clouds against precipitation depletion. *Journal of Geophysical Research: Atmospheres*, *129*, e2023JD039572. https://doi.org/10.1029/2023JD039572

Received 5 JULY 2023
Accepted 10 JUN 2024

Author Contributions:

Conceptualization: Isabel L. McCoy, Matthew C. Wyant, Peter N. Blossey, Christopher S. Bretherton, Robert Wood
Data curation: Isabel L. McCoy, Matthew C. Wyant, Peter N. Blossey
Formal analysis: Isabel L. McCoy, Matthew C. Wyant, Peter N. Blossey
Funding acquisition: Isabel L. McCoy, Peter N. Blossey, Christopher S. Bretherton, Robert Wood
Investigation: Isabel L. McCoy, Matthew C. Wyant, Peter N. Blossey, Christopher S. Bretherton, Robert Wood

Abstract Aerosol-cloud-precipitation interactions are a leading source of uncertainty in estimating climate sensitivity. Remote marine boundary layers where accumulation mode (~100–400 nm diameter) aerosol concentrations are relatively low are very susceptible to aerosol changes. These regions also experience heightened Aitken mode aerosol (~10–100 nm) concentrations associated with ocean biology. Aitken aerosols may significantly influence cloud properties and evolution by replenishing cloud condensation nuclei and droplet number lost through precipitation (i.e., Aitken buffering). We use a large-eddy simulation with an Aitken-mode enabled microphysics scheme to examine the role of Aitken buffering in a mid-latitude decoupled boundary layer cloud regime observed on 15 July 2017 during the Aerosol and Cloud Experiments in the Eastern North Atlantic flight campaign: cumulus rising into stratocumulus under elevated Aitken concentrations (~100–200 mg^{-1}). In situ measurements are used to constrain and evaluate this case study. Our simulation accurately captures observed aerosol-cloud-precipitation interactions and reveals time-evolving processes driving regime development and evolution. Aitken activation into the accumulation mode in the cumulus layer provides a reservoir for turbulence and convection to carry accumulation aerosols into the drizzling stratocumulus layer above. Further Aitken activation occurs aloft in the stratocumulus layer. Together, these activation events buffer this cloud regime against precipitation removal, reducing cloud break-up and associated increases in heterogeneity. We examine cloud evolution sensitivity to initial aerosol conditions. With halved accumulation number, Aitken aerosols restore accumulation concentrations, maintain droplet number similar to original values, and prevent cloud break-up. Without Aitken aerosols, precipitation-driven cloud break-up occurs rapidly. In this regime, Aitken buffering sustains brighter, more homogeneous clouds for longer.

Plain Language Summary Aerosols, small particles in the atmosphere associated with ocean biology, sea spray, land, and human-produced emissions, influence cloud brightness and, by suppressing precipitation and subsequent break up, cloud lifetime. Understanding aerosol-cloud-precipitation interactions is critical in understanding how aerosols influence the climate system. This study examines how the very smallest aerosol particles modify cloud formation, brightness, and lifetime over the North Atlantic ocean. We utilize a recent set of aircraft and satellite observations from a dedicated field campaign as well as a detailed model that resolves fine-scale interactions important to cloud development. After comparing the model to real-world observations, we test how modifying the amount of small particles impacts the cloud brightness and lifetime. We find that the small particles are able to offset precipitation removal of larger particles, helping clouds to last longer and stay brighter.

1. Introduction

Recently, liquid cloud aerosol-cloud interactions (aci) have been identified as a key, remaining source of uncertainty in accurately estimating climate sensitivity (Bellouin et al., 2020). Aci impacts the climate system in two ways (Bellouin et al., 2020; Boucher et al., 2013; Christensen et al., 2022; Wood, 2012). The first is through radiative forcing (RF_{aci}), which manifests as a change in cloud droplet number concentration (N_d) in response to a change in aerosol while other macrophysical characteristics (e.g., liquid water content, LWC) remain constant (Twomey, 1977): increasing aerosol amount leads to increasing N_d and an increase in the fraction of shortwave reflected back to space (i.e., albedo) associated with the accompanying reduction in surface area per droplet. The

Methodology: Isabel L. McCoy, Matthew C. Wyant, Peter N. Blossey, Christopher S. Bretherton, Robert Wood
Project administration: Isabel L. McCoy, Peter N. Blossey, Christopher S. Bretherton, Robert Wood
Resources: Isabel L. McCoy, Peter N. Blossey, Christopher S. Bretherton, Robert Wood
Software: Isabel L. McCoy, Matthew C. Wyant, Peter N. Blossey
Supervision: Isabel L. McCoy, Peter N. Blossey, Christopher S. Bretherton, Robert Wood
Validation: Isabel L. McCoy, Matthew C. Wyant, Peter N. Blossey, Robert Wood
Visualization: Isabel L. McCoy, Matthew C. Wyant, Peter N. Blossey
Writing – original draft: Isabel L. McCoy
Writing – review & editing: Isabel L. McCoy, Matthew C. Wyant, Peter N. Blossey, Christopher S. Bretherton, Robert Wood

second is through cloud adjustments, which manifest as a change in cloud macrophysical characteristics (e.g., cloud liquid, amount, thickness, etc.) through changes in cloud microphysics (e.g., precipitation, evaporation, etc.) (e.g., Ackerman et al., 2004; B. A. Albrecht, 1989; Bretherton et al., 2007; S. Wang et al., 2003; Xue & Feingold, 2006). These combined effects in response to a change in aerosol (i.e., from the pre-industrial aerosol state to the present day) are known as the effective radiative forcing (ERF_{aci}).

Global climate models (GCMs) have particular difficulty in capturing aci in cloud regimes that are biologically active with little anthropogenic influence (e.g., Carslaw et al., 2013; McCoy et al., 2020). Some of this is likely due to incomplete representation of Aitken aerosol production and its contribution to aci (Gordon et al., 2017; McCoy et al., 2021). Aitken aerosols (∼10–100 nm in diameter) form through various processes including gas to particle conversion from ocean biology emissions (Seinfeld & Pandis, 2016) which can occur at cloud edges (e.g., Clarke et al., 1998; Kazil et al., 2011), continental anthropogenic emissions (e.g., Twohy et al., 2002), and, in recent studies, from sea spray production (Lawler et al., 2021; Xu et al., 2022). They have been observed in high concentrations in the free troposphere (FT) intermittently across the globe (Williamson et al., 2019). In the boundary layer (BL), where they are sometimes generated (Zheng et al., 2021), Aitken particles act as a key source of accumulation mode aerosol (∼100–400 nm) (e.g., Covert et al., 1996; Sanchez et al., 2018; Zheng et al., 2018). Accumulation mode aerosols are then activated in moist updrafts into cloud condensation nuclei (CCN). Enhanced supersaturation (Kaufman & Tanré, 1994) and updraft strength (Pöhlker et al., 2021), particularly in the absence of accumulation mode particles, can facilitate activation of smaller, Aitken particles into CCN as well (Fan et al., 2018).

Aitken mode-aerosols may have an additional role to play in aerosol-cloud-precipitation interactions. Drawing on Southern Ocean observations, McCoy et al. (2021) recently hypothesized that Aitken particles buffer precipitating BL clouds against cloud droplet depletion: as precipitation removes accumulation mode aerosol, peak supersaturation increases in updrafts, and larger aerosols in the Aitken mode are able to activate into CCN with the potential to grow larger, restoring N_d. This buffering mechanism is consistent with the idea that changes in cloud-active aerosol can be partially compensated when changes in aerosol composition and size distributions lead to increased supersaturation and thus increased activation of smaller condensation nuclei (e.g., "microphysical buffering," Stevens & Feingold, 2009; Twomey, 1959). During the biologically-active Southern Ocean Austral summer, Aitken aerosol are plentiful both in a substantial FT reservoir developed through synoptic-scale uplift and in the BL as a result of synoptic-scale descent (Covert et al., 1996; McCoy et al., 2021). Southern Ocean clouds have been observed to have many fewer optically-thin cloud features than in similar clouds observed in the Northeast Pacific stratocumulus (Sc) to cumulus (Cu) transitions that were experiencing similar accumulation mode concentrations but lower Aitken mode concentrations (McCoy et al., 2021; O, Wood, & Tseng, 2018). In the sub-tropics, these features are generated in association with precipitation-driven depletion of the cloud droplet and accumulation mode aerosol populations (O, Wood, & Bretherton, 2018; O, Wood, & Tseng, 2018; Wood et al., 2018). Less frequent occurrence of optically-thin cloud features in the Southern Ocean is thus consistent with a damping of precipitation processes by Aitken-buffering.

Recent large-eddy simulation (LES) and observational studies have found Aitken aerosols impact cloud microphysical and radiative properties in pristine environments (Pöhlker et al., 2021; Wyant et al., 2022), although their influence is modulated by cloud phase (Bulatovic et al., 2021). In particular, Wyant et al. (2022, hereafter W22) developed an Aitken-mode enabled microphysics scheme that predicts time evolution of aerosol-cloud-precipitation interactions by including aerosol sinks and sources (albeit neglecting new particle formation). W22 utilized an idealized Southeast Pacific case study of deep, precipitating Sc informed by in situ observations to directly evaluate the Aitken-buffering hypothesis. They simulated this case over several days, finding a gradual loss of accumulation mode aerosol to drizzle formation led to a transition to an ultra-clean, low cloud fraction, and strongly precipitating Cu state. This transition could be delayed by increasing Aitken concentrations above the inversion or through fluxes from the surface.

The Aitken-buffering mechanism, which has both observational (McCoy et al., 2021) and modeling (Wyant et al., 2022) support, has important implications for our understanding of aci as well as past and future climates. Konsta et al. (2022) recently found that the "too few, too bright" bias in GCMs has persisted in many state-of-the-art models largely due to GCMs' difficulty in capturing the heterogeneity of clouds at lower cloud fractions. Specifically, GCMs fail to represent the wide-spread occurrence of optically-thin cloud features (Konsta et al., 2022) that occur across a variety of mesoscale cloud morphology patterns (Leahy et al., 2012; McCoy,

McCoy, et al., 2023; Mieslinger et al., 2021; O, Wood, & Tseng, 2018) and may depend in part on the absence of Aitken aerosols (McCoy et al., 2021). Variations in optically-thin cloud amount across morphology patterns contributes to differences in their cloud radiative impact and how we expect them to feed back on the climate system under climate change (McCoy, McCoy, et al., 2023). Incomplete representation of Aitken aerosol processes in GCMs may also influence our estimation of RF_{aci} and therefore ERF_{aci} as Aitken aerosols may play a critical role in regulating N_d in pristine, pre-industrial environments (Gordon et al., 2016, 2017; McCoy et al., 2020). Thus, identifying the key processes involved in aerosol-cloud-precipitation interactions driven by Aitken aerosols and understanding their nuances has utility in improving both our knowledge of the climate system and the representation of cloud-aerosol interactions in models used for climate prediction.

In this study, we build on the work of W22 by utilizing their Aitken-enabled microphysics scheme in large eddy simulations (Section 2.2) to examine the influence of Aitken aerosols on an observationally-constrained case study sampled during the recent Aerosol and Cloud Experiments in the Eastern North Atlantic (ACE-ENA) flight campaign in the Northeast Atlantic (J. Wang et al., 2022). Specifically, we examine a case of Cu rising into Sc under substantial Aitken aerosol concentrations that was sampled by aircraft on 15 July 2017. We extend W22 by using these in situ observations (Section 2.1) to constrain the LES control simulation (Section 3.1). Successful simulation of this case allows us to identify the key processes involved in the evolution of clouds in such a regime (Section 3.2). Aerosol sensitivity studies are conducted (Section 4) to examine the dependence on initial aerosol state and subsequent nuances of rapid aerosol processing, changes in cloud microphysics, radiative properties, and heterogeneity (as measured by the development of optically-thin cloud features). We especially focus on the influence of Aitken aerosols on cloud properties under this meteorologically-forced regime. We conclude with a discussion (Section 5) and summary (Section 6).

2. Data and Methods

2.1. Observations for the ACE-ENA Case Study

In situ observations from the 15 July 2017 flight (Figure 1) during the summer phase of the ACE-ENA campaign (J. Wang et al., 2022) form the basis for our LES case study. This research flight by the Department of Energy G-1 aircraft (hereafter RF16 of the campaign) sampled a system of Cu (bases at ∼500 m) rising into Sc (∼1,000–1,500 m) to the northwest of Graciosa Island (Figure 1). This system gradually advected to the southwest over the day (e.g., Figure 2b in J. Wang et al. (2022)). The G-1 aircraft utilized a Lagrangian-drift sampling pattern consisting of multiple stacked level legs ∼60 km in length. Each leg followed a straight, crosswind line at altitudes set to sample above, in, and below cloud and ended in a vertical ascent profile to the next level leg altitude (Figure 1b). ERA5 reanalysis extracted for the ACE-ENA campaign region show that, over the course of the day, the atmosphere experienced increasing large-scale uplift (Figure S3a in Supporting Information S1) and an associated cooling and moistening by large-scale vertical advection (Figures S3b and S3c in Supporting Information S1). Mesoscale moisture convergence (e.g., Bretherton & Blossey, 2017) can be encouraged by large-scale uplift (e.g., as seen in trade-wind clouds, Narenpitak et al., 2021), and may contribute to the deepening and moistening of clouds observed in this case.

The G-1 aircraft was outfitted with a suite of instruments, a subset of which we utilize to both develop and compare with our LES case study. The Fast Integrated Mobility Spectrometer (FIMS, J. Wang et al., 2017) and the Passive Cavity Aerosol Spectrometer Probe (PCASP) provide size distributions and number concentrations for Aitken (∼10–100 nm) and accumulation (∼100–400 nm) mode size ranges, respectively. The FIMS resolves the full 10–400 nm size range while the PCASP resolves the larger, accumulation sizes only (e.g., Figure 4). Total aerosol number concentrations for this study are calculated as the sum of the Aitken and accumulation number concentrations from these specified size ranges, which is found to be similar to the observations from the Condensation Particle Counter (CPC, sizes ≥10 nm, not shown). The Fast Cloud Droplet Probe (FCDP) is used for cloud N_d and LWC. Precipitation flux, which includes cloud droplet sedimentation, is calculated from droplet spectra measurements assuming terminal fall-speeds from Rogers and Yau (1989). Spectra are based on two instruments that optimally sample different drop size ranges (results are not sensitive to the diameter cutoff): the FCDP (selecting diameters ≤50 μm) and the Two-Dimensional Stereo Particle Imaging Probe (2DS, diameters ≥50 μm).

For the model-observation comparison, we focus on the second half of the flight period (12:00–14:30 UTC). Note that local solar time is ∼2 hr behind UTC. This portion of the flight was cloud-rich and generally moister than the

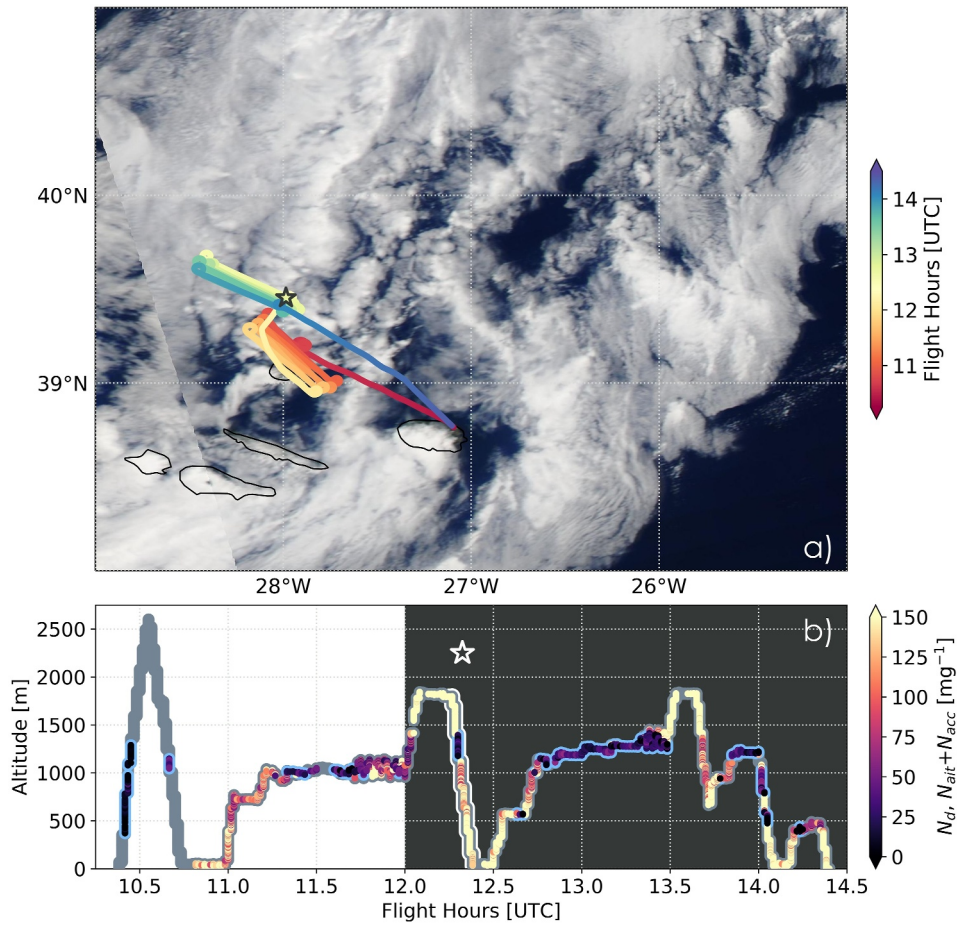

Figure 1. (a) MODIS *Aqua* visual imagery on 15 July 2017 at 14:30 UTC or 13:30 local time with the RF16 flight path colored by time. (b) Flight altitude versus UTC time (gray) with color overlay of observations (where available) of total aerosol from simultaneously sampled $N_{ait} + N_{acc}$ or, in cloud, N_d. In cloud sampling, where liquid water content $\geq$0.01 g kg^{-1}, is outlined in blue. The dark gray background from 12:00 to 14:30 UTC is the observational comparison period used in model evaluation. Separately plotted N_{ait} and N_{acc} versions are shown in Figure S1 of Supporting Information S1. The profile used for initializing aerosol is marked with a star in (a), (b) and outlined in white in (b).

first, drier half (see blue outlines, Figure 1b). Aitken and accumulation aerosol size ranges are simultaneously sampled more consistently in the second half as well (shown separately in Figure S1 of Supporting Information S1 and as a sum, when both are sampled, in Figure 1b). Aerosol comparison levels are selected to be further from clouds (where observations are sparse). The profile at ~12:15 p.m. (profile 2, P2) sampled the depth of the BL and is used as the initial LES aerosol profile (star in Figure 1 and Figure S1 in Supporting Information S1, discussed further in Section 2.2).

We also compare our results against cloud liquid water path (LWP), cloud optical depth (τ), and broadband albedo retrievals for the ACE-ENA campaign (ARM Data Center, 2017) from the NASA SATCORPS (Satellite Cloud Observations and Radiative Property retrieval System) product which applies the VISST (Visible Infrared Solar-infrared Split-Window Technique) algorithm to Meteosat-10 satellite channels (Minnis et al., 2001, 2008, 2011). The broadband albedo retrieval product includes a correction based on converting to shortwave flux and regionally (5° × 5°) normalizing to Edition 4 of the CERES (Clouds and the Earth's Radiant Energy System) *Aqua* SSF1deg product for the corresponding month. We utilize these satellite products to provide further insight into the aerosol-cloud-precipitation system sampled by the aircraft. Thus, model-satellite comparisons are also restricted to 12:00–14:30 UTC. LES output is coarsened to the SATCORPS temporal (0.5 hr) and spatial (~3 km) resolutions. In order to capture a representative sample of this case's cloud heterogeneity while restricted to the coarser satellite resolution, we use a 2° × 2° domain overlapping the flight region (27°–29°W and 39–41°N,

Figure 1a and Figure S2 in Supporting Information S1). We sub-sample this into 49 sub-domains of comparable area to the LES simulation domain (~0.25° × 0.25°, see Figure S2b in Supporting Information S1 for an example). This is a sufficient sample size to facilitate statistical comparisons between the LES and the various cloud system realizations captured by the satellite subdomains.

2.2. Aitken-Aerosol-Enabled Large-Eddy Simulations

We utilize W22's novel two-mode aerosol microphysics scheme for the System for Atmospheric Modeling (SAM) LES simulations (25.6 × 25.6 km^2 domain with 100 m resolution). This Hoppel Transfer scheme extends the single-mode, two-moment prognostic aerosol scheme of Berner et al. (2013) by including Aitken aerosol evolution and a simple representation of sulfur chemistry. Seven prognostic variables represent accumulation and Aitken log-normal aerosol modes in air and droplets as well as three gas species (H_2SO_4, SO_2, and DMS). Scavenging of interstitial and other unactivated aerosol by cloud and rain drops are treated as in Berner et al. (2013), while coagulation of unactivated aerosols follow Binkowski and Shankar (1995). A simplified scheme for capturing basic influences of sulfur chemistry on model aerosols is also included, but new particle formation (e.g., aerosols nucleating from gas-phase H_2SO_4) is neglected for simplicity (unlike in Kazil et al. (2011)). The only sources of Aitken aerosols considered in the scheme are from surface fluxes and entrainment from the FT. Two aerosol modes are used to approximately capture the Aitken (~10–100 nm) and accumulation (~100–400 nm) modes, though it should be noted that the characteristic modal diameter of each aerosol mode can evolve in response to aerosol and chemical processes.

The premise of the W22 Hoppel Transfer scheme is to allow activation of Aitken mode particles in saturated updrafts so that they can act as CCN in the model. When — during activation — the number of Aitken particles at the critical diameter exceeds the number of accumulation mode particles, aerosols are shifted from the Aitken to the accumulation mode to enforce equality between the Aitken and accumulation mode concentrations at the critical diameter. Conceptually, this should place the Hoppel minimum (D_{Hoppel}) at the critical diameter (D_c) in strong updrafts. In weak updrafts, where D_c is larger than D_{Hoppel}, no Aitken particles are moved into the accumulation mode. For simplicity, we assume that all cloud droplets are associated with an accumulation mode aerosol, so the "Aitken" mode is composed of unactivated aerosols. Supersaturation, which helps to determine D_c, is diagnostic and computed within the Morrison microphysics scheme (Morrison et al., 2005; Wyant et al., 2022). Typical supersaturation values experienced by CCN upon activation (i.e., mean supersaturation weighted by local activation rate) range across the BL from 0.13% to 0.26% for accumulation mode aerosols and 0.23%–0.35% for Aitken mode aerosols transferred into the accumulation mode, comparable to the range of maximum supersaturations (0.1%–0.3%) observed in this region during the summer of 2017 (Gong et al., 2023). The typical updraft strengths during activation range from ~0.2 to 0.6 m s^{-1} for accumulation and ~0.5–1.0 m s^{-1} for Aitken mode aerosols.

As in W22, all aerosols are assumed soluble with the dry density and hygroscopicity of ammonium sulfate (i.e., $B = 0.51$ in Eq. 3 of Abdul-Razzak and Ghan (2000)). This is broadly consistent with the ACE-ENA time-of-flight aerosol mass spectrometer observations of bulk non-refractory aerosol composition showing the summertime marine BL was dominated by sulfate mass (J. Wang et al., 2022). We additionally note that in the W22 formulation, transferred Aitken mode aerosols are instantaneously shifted to larger sizes (due to refitting the log-normal accumulation mode after transfer). While the instantaneous growth of the transferred aerosols is unrealistic, one would expect such particles to grow over time due to aqueous sulfate deposition (Kaufman & Tanré, 1994). Unlike other schemes that explicitly capture sulfate growth through allowing Aitken sized particles to grow into cloud and return to Aitken mode sizes (e.g., Feingold et al., 1996; Ivanova & Leighton, 2008a; Ivanova & Leighton, 2008b), for computational efficiency we approximate Aitken activation as a transfer to the accumulation mode as soon as activation occurs. Following Kaufman and Tanré (1994), it is likely sulfate uptake depends on cloud droplet size (not on embedded aerosol size) and initially smaller aerosols will experience greater growth than larger aerosols. Due to our bulk treatment of aerosol chemistry and use of a fixed shape parameter, differential growth of smaller aerosols is not possible. However, this growth effect appears in the transfer albeit at a shorter timescale and for somewhat artificial reasons.

A key distinction between this study and the more idealized W22 study is that our LES case is more tightly constrained by in situ observations in an effort to simulate aerosol-cloud-precipitation interactions in a context as similar to the real world as possible. Initial thermodynamic profiles of temperature and moisture are developed

from a combination of the Graciosa Island soundings, ERA5 reanalysis soundings extracted to the campaign region (Figure S3 in Supporting Information S1), and in situ flight profiles. As initial simulations produced thinner-than-observed clouds, the moisture profiles were slightly enhanced to better correspond with the second, comparison portion of the observations (12:00–14:30 UTC) (Figure 1b; Figures S1 and S5b in Supporting Information S1). The initial Aitken and accumulation mode aerosol number and mass mixing ratios (Figure S4a, S4b, S5c, and S5d in Supporting Information S1) follow the P2 reference profile from RF16 (star in Figure 1). Modal Aitken and accumulation widths (as defined by geometric standard deviation, $\sigma_{ait} = 1.3$ and $\sigma_{acc} = 1.4$ μm) and initial diameters (Table S1 in Supporting Information S1) are selected to correspond to case observations (Figure S4c in Supporting Information S1). While the characteristic diameter of each aerosol mode may evolve, the modal widths are fixed in time. The initial SAM modes and the observed size distributions for P2 are shown in Figure S6 of Supporting Information S1, initial values are detailed in Table S1, Figures S5c, and S5d in Supporting Information S1. N_d is initialized at 35 mg^{-1} based on the median in situ observations for the upper cloud layer (Figure S4d in Supporting Information S1).

Simulations are initialized with a small, random moisture and temperature perturbation and run for 12 hr to allow the development of mesoscale variability. During this period, the domain-mean profiles of temperature, specific humidity, aerosol number and mass mixing ratios below cloud top (~1,175 m) are nudged to the previously discussed, initial profiles (Figure S5 in Supporting Information S1) that capture key elements of the RF16 environment. A 10 min nudging timescale is used for all nudging above cloud top. Below cloud top, aerosols are nudged with a 10 min timescale, while the moisture and temperature fields are nudged on a longer 1 hr timescale to allow for the development of mesoscale organization. An exception is made below 500 m where the inverse nudging timescale applied to temperature and moisture decreases gradually to zero at the surface. Weaker nudging in the subcloud layer allows surface-flux-driven turbulence and convection to develop during the spinup period. Afterward, nudging within the BL and the inversion layer is switched off so that the simulations are released to run freely at 9:00 UTC and throughout the remaining 12 hr duration of the simulation (ending at 21:00 UTC). Following Blossey et al. (2021), after release each simulation is forced by the large-scale vertical velocity as well as moisture and temperature tendencies from ERA5 to maintain meteorology at real world conditions throughout the simulation, while nudging to the initial profiles only in the FT at a timescale of 30 min starting 500 m above the inversion. Although aerosols are affected by large-scale vertical motion, no large-scale horizontal advective tendencies are applied to the aerosol, so that, after a simulation is released, the aerosol evolves as a net balance between sources and sinks as in, for example, Wood (2006).

Surface fluxes of momentum, heat and moisture are computed interactively using bulk schemes in SAM. Surface aerosol fluxes follow the approach in W22, which depend on the 10 m wind speed ($u_{10} \sim 2$ m s^{-1}, Figure S3d in Supporting Information S1) raised to the 3.41 power and are thus very small in this case. A damping layer is applied above 2 km altitude, and the model top is set at 2.9 km. Radiative heating is computed by RRTMG (Mlawer et al., 1997) over the full atmospheric column by joining the model profiles with those from the forcing data set above the mode. While the case study is Eulerian, the domain is translated with a fixed velocity (u, $v = -2$ m s^{-1}) to minimize cross-grid flow (Wyant et al., 2018).

For model-observation comparisons, SAM aerosol number concentrations are calculated as in Zender (2001) using aerosol size distributions truncated to specific instrument observation size ranges for Aitken (10–100 nm), accumulation (100–400 nm), and total (combined Aitken and accumulation ranges, 10–400 nm) aerosol. Where necessary, SAM profiles compared to observations are subset to in-cloud (LWC ≥ 0.01 g kg^{-1}) and out-of-cloud (<0.01 g kg^{-1}) samples (e.g., observed aerosol concentrations are only reported out-of-cloud while droplet number concentrations are only reported in-cloud). All size distributions from SAM are computed for the combined in- and out-of-cloud aerosol across the $x - y$ domain for each time and height level. For comparisons with observed size distributions, we have selected relatively cloud-free altitudes (i.e., the lower BL at 300 m, the transition layer between Cu and Sc cloud layers at 700 m, and the FT at 1.6 km). When comparing across sensitivity studies, distributions at altitudes dominated by cloud (i.e., 0.5, 1, and 1.4 km) and aerosol budgets are also included in order to directly examine aerosol-cloud processing. Precipitation fluxes are calculated as the integral of sedimentation fluxes over cloud and rain droplet sizes, equivalent to observations.

The evolution of aerosol-cloud precipitation interactions are examined using number and mass budgets for Aitken and accumulation modes over several atmospheric layers. These budgets are formulated following W22. The accumulation mode in this context is composed of unactivated accumulation, in-cloud droplet, and in-rain

aerosols. Thus, activation and droplet evaporation (which leaves behind unactivated accumulation mode aerosols) do not have a net impact on the budget. For each aerosol category, the number tendencies evolve following a rate equation:

$$\dot{N}_{Tot.} = \dot{N}_{Ait.\ Trans.} + \dot{N}_{Top\ Flux} + \dot{N}_{Bot.\ Flux} + \dot{N}_{Wet\ Scav.} + \dot{N}_{Scav.} + \dot{N}_{Coag.} + \dot{N}_{Large\text{-}Scale\ Vert.\ Mot.} + \dot{N}_{Sed.} + \dot{N}_{Nudge.} + \dot{N}_{Res.} \quad (1)$$

This can be further simplified as:

$$\dot{N}_{Tot.} = \dot{N}_{Ait.\ Trans.} + \dot{N}_{Top\ Flux} + \dot{N}_{Bot.\ Flux} + \dot{N}_{Wet\ Scav.} + \dot{N}_{Other} + \dot{N}_{Res.} \quad (2)$$

The leading terms are activation or transfer of Aitken aerosol into the accumulation mode (*Aitken Transfer*), movement of aerosol through turbulent fluxes (*Top Flux* and *Bottom Flux* relative to the layer the budget is computed over), and removal of aerosol through autoconversion, accretion, and limiters (as in Berner et al., 2013, *Wet Scavenging*). Tendency terms with small contributions are gathered for analysis purposes into the *Other* term. These are scavenging (in-cloud removal of interstitial and unactivated aerosol), coagulation (removal of aerosol through coalescence or aggregation of aerosols via Brownian motion), aerosol transport by large-scale vertical motion, sedimentation of aerosols out of the atmosphere, and nudging tendencies applied during the spin-up phase of the model (before 9:00 UTC). The residual captures the remaining behavior of the total aerosol tendencies and, when small, indicates that these equations capture the majority of the aerosol behavior. Note that the meaning of the turbulent fluxes changes depending on the layer they are computed over (i.e., surface source, exchange between layers). The mass budgets have a similar formulation with an additional term for chemistry (particle growth through chemical processing):

$$\dot{M}_{Tot.} = \dot{M}_{Chem.} + \dot{M}_{Ait.\ Trans.} + \dot{M}_{Top\ Flux} + \dot{M}_{Bot.\ Flux} + \dot{M}_{Wet\ Scav.} + \dot{M}_{Scav.} + \dot{M}_{Coag.} + \dot{M}_{Large\text{-}Scale\ Vert.\ Mot.} + \dot{M}_{Sed.} + \dot{M}_{Nudge.} + \dot{M}_{Res.} \quad (3)$$

Time evolution for all number and mass budget terms are shown in the supplement (Figures S7 and S8 in Supporting Information S1, respectively).

Aerosol sensitivity studies, described in Section 4, adjust the initial number concentration profiles. In each case, corresponding changes are made to the initial mass profiles so that the initial diameter and width of modes are identical across all simulations (Table S1 in Supporting Information S1). These changes to the initial aerosol profiles include halving the accumulation number while leaving the Aitken mode unchanged (*HfAc*), eliminating the Aitken mode while leaving the accumulation mode unchanged (*NoAit*), and halving the accumulation mode number while eliminating the Aitken mode (*HfAcNoAit*). To avoid computational issues, when Aitken aerosol is removed in the *NoAit* and *HfAcNoAit* simulations, Aitken number and mass are set to small, non-zero values. In the *HfAc* and *HfAcNoAit* simulations, both accumulation mass and number are halved relative to the vertically resolved *Ctrl* initial profile.

Three additional sensitivity studies are conducted that do not alter the initial aerosol profiles but instead test the sensitivity to other aspects of the simulation set up. These are examined in Appendix A. *Ctrl LD* examines the dependence of the *Ctrl* simulation on domain by doubling its size. Additionally, we conduct two studies, *AltHopV1* and *AltHopV2*, to examine the sensitivity of the *Ctrl* to variations in the W22 Hoppel Transfer scheme.

3. Simulating the RF16 ACE-ENA Case Study

We first present the general behavior of the standard SAM simulation for RF16 (hereafter *Ctrl*, Section 2.2). Figure 2 shows the evolution of aerosol and cloud droplet number along with the corresponding changes to horizontal variations in τ. Consistent with observations, two cloud layers form: an upper, Sc layer between ~1–1.5 km altitude and a shallow, Cu layer near the surface (~400–600 m). N_{ait} remains high in the FT and is initially (~10:00 UTC) large throughout the BL (Figure 2a). N_{acc} has the opposite structure (d). Over time, the Cu in the lower layer intensifies and drives local changes in aerosol size distributions (N_{ait} reduces while N_{acc} increases, b and e), increases in N_d (h) as larger cumuli connect (e.g., 12:00, b, e, h) and rise into the upper Sc layer (e.g., 14:00

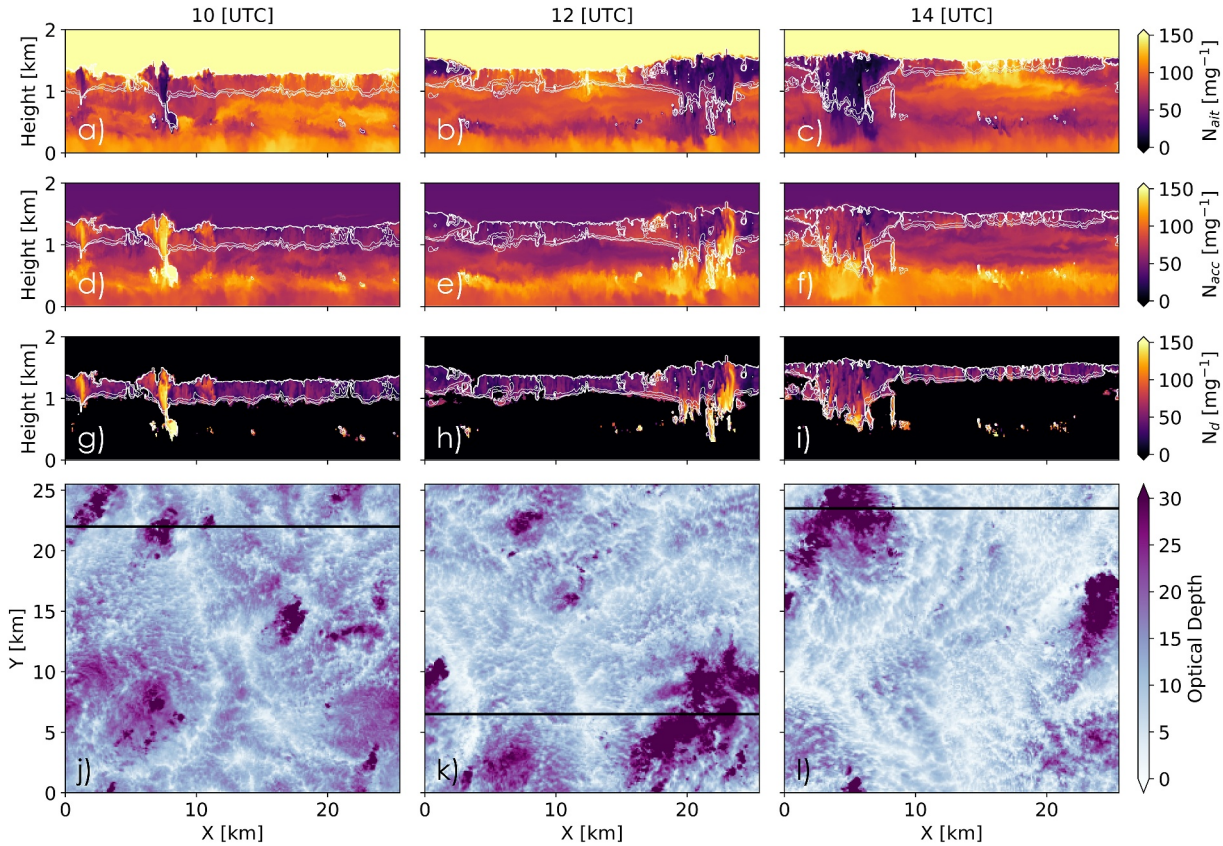

Figure 2. Vertical cross sections of SAM *Ctrl* simulation for Aitken (a–c), accumulation (d–f), and cloud droplet (g–i) number concentrations at (a, d, g) 10:00, (b, e, h) 12:00, and (c, f, i) 14:00 UTC. Corresponding cloud optical depth spatial *x*-*y* snapshots for (j) 10:00, (k) 12:00, and (l) 14:00 UTC. The black lines in (j–l) shows the location of vertical cross sections shown in (a–i).

UTC, c, f, i). The upper layer deepens with time as Sc clouds grow larger and are fed by the Cu below. Sc cells become more well defined (e.g., 14:00 UTC) with increased core N_d (h, i) and τ (k, l). Large-scale uplift (Figure S3a in Supporting Information S1) may influence this cloud evolution as well. The *Ctrl* simulation captures the stratified aerosol vertical distribution evident in the RF16 observations. N_{ait} is largest in the FT (Figures S1a and S4a in Supporting Information S1) and contributes the most to the total aerosol magnitude (Figure 1b), significantly exceeding N_{acc} at most heights in the marine BL (Figures S1b and S4a in Supporting Information S1) as will be discussed further in Section 3.1. Our simulations will facilitate further examination of essential aerosol-cloud-precipitation processes at work in this decoupled low cloud regime (Section 3.2).

3.1. Observational Evaluation

Interrogating the *Ctrl* simulation with observations (Section 2.1 and 2.2) informs us of the capabilities and limitations of our case study and model. Skill in reproducing the net behavior sampled during RF16 will give us confidence in our ability to capture the complex interplay of aerosol-cloud-precipitation processes driving the cloud system evolution in this regime.

Our first evaluation utilizes vertical profiles of several key quantities observed from the G-1 aircraft over the comparison period (12:00–14:30 UTC, Figure 3). The *Ctrl* median and interquartile range are compared with the observed median and interquartile range in 10 altitude bins (which are used to account for differences in aircraft sampling frequency across the BL). Generally, median *Ctrl* profiles fall within the interquartile range of observed profiles, demonstrating the skill of our simulation. Because the simulated aerosol state, which has very good agreement with observed out-of-cloud aerosol (Figures 3a–3c) is critical in our study, it is worth examining in more detail.

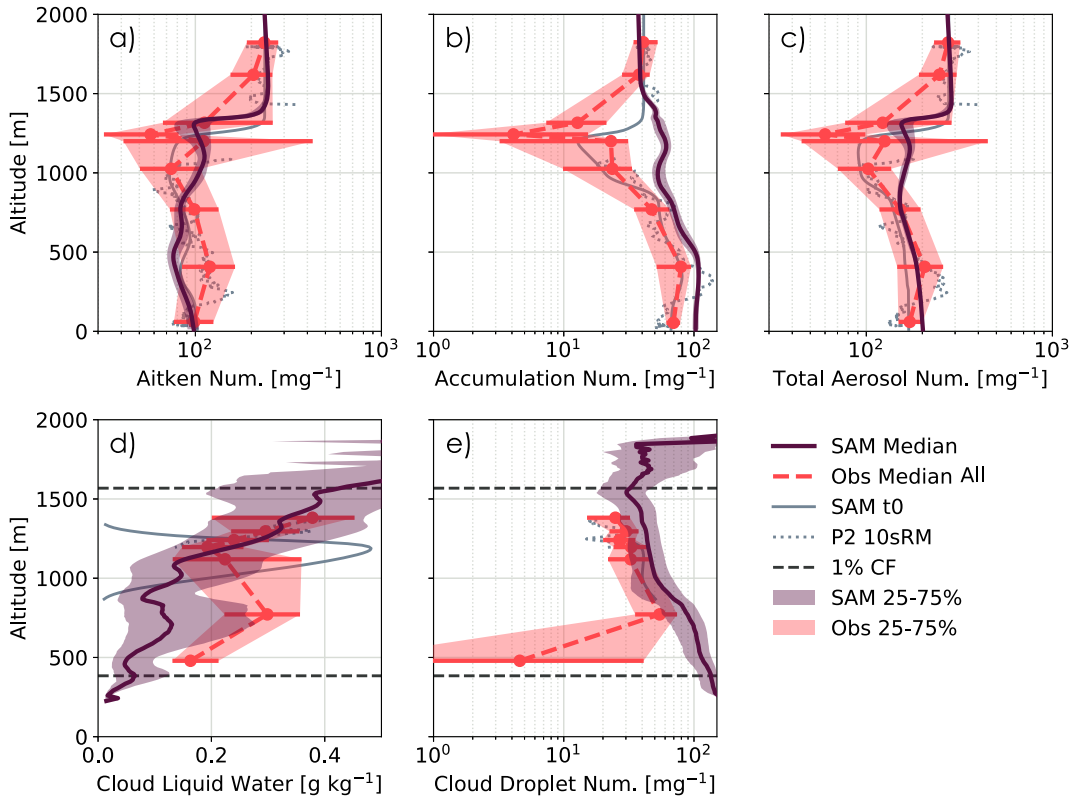

Figure 3. Model-observation comparison of median vertical profiles for select variables over 12:00–14:30 UTC: number concentrations of (a) Aitken mode, (b) accumulation mode, (c) total aerosol (the sum of accumulation and Aitken aerosol modes), and (e) cloud droplets; and (d) cloud liquid water content (LWC). Aerosol comparisons are computed only for out-of-cloud samples while cloud LWC and droplets are only for in-cloud samples. Observations (red) are binned into 10 quantiles by altitude and shown as a median (dashed line with dots) and an interquartile range (shading with horizontal lines) for each bin. SAM *Ctrl* (purple) is similarly shown as a median (line) with interquartile range (shading). Initial estimates are included for the observations (10-s running mean for profile 2, dashed gray) and SAM (simulation profile after spinup period at 9:00 UTC as in Figure S5 of Supporting Information S1, solid gray). The cloud layer edges in SAM, where median cloud fraction is 1%, are included for reference as dark gray, dashed horizontal lines in (d) and (e).

Total aerosol number concentrations (Figure 3c), the sum of Aitken and accumulation number (Figures 3a and 3b), coincide with observations across all altitudes and have one of the best overall agreements of all the variables examined. When aerosol number is separated into its individual modes, good agreement is still found across most altitudes for accumulation and across all altitudes for Aitken concentrations. Opposing deviations away from observed behaviors are seen in the Aitken and accumulation size ranges in the BL near ~500 m in the Cu layer: simulated Aitken aerosol number (Figure 3a) is slightly depleted but still within the interquartile range while accumulation number (Figure 3b) is augmented relative to observations. In addition to their slight deviation near the Cu (~0–500 m), accumulation concentrations deviate by a factor of ~2× in the Sc layer (~1–1.5 km, e.g., Figures 2e and 2f), falling outside of the observed interquartile ranges in both cloud layers. Note that there are large observational uncertainties in the upper cloud layer as observations at this altitude are impacted by limited opportunities for in situ aerosol sampling in cloud-free air.

Even though the Cu and Sc cloud layers occur in both observations and SAM (e.g., Figure 1b, sparse quantiles near ~500 m and numerous quantiles between 1 and 1.5 km, Figures 3d and 3e), the modal aerosol partitioning does not exactly match. The slight depletion of Aitken aerosol (Figures 2a–2c) and the accompanying increase in accumulation mode aerosol (Figures 2d–2f) indicates sufficient updraft strength and supersaturation occurs in the nearby, thin Cu layer to enable Aitken activation through the W22 Hoppel Transfer scheme. This can also be seen in the evolution of the simulated aerosol size distribution at 300 m from its initial shape to its median behavior over the observation-comparison period (Figure 4c). The characteristic modal diameter for the Aitken mode

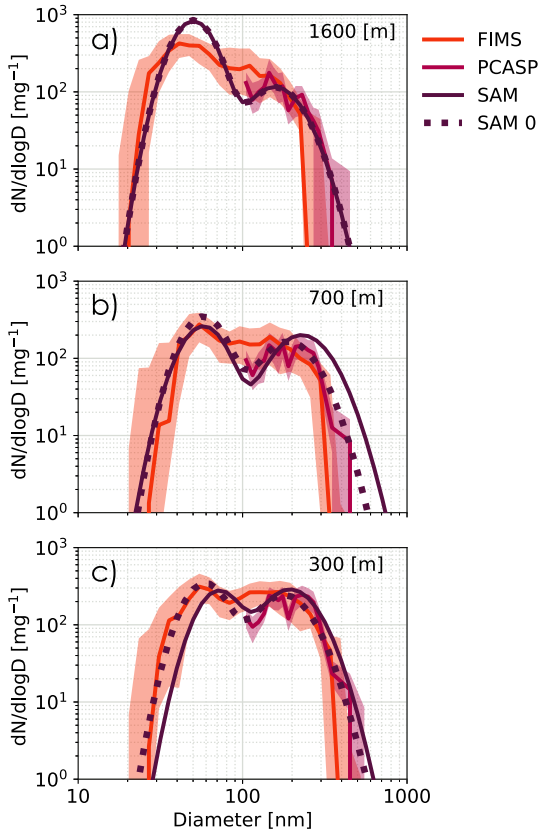

Figure 4. Model-observation comparison of median aerosol size distributions over 12:00–14:30 UTC at three levels: (a) 1,600 m, (b) 700 m, and (c) 300 m. Observations within 100 m of the labeled SAM altitude level are included. SAM *Ctrl* size distributions (purple) for the initial (dashed, Section 2.2) and comparison period median (solid) are shown. Inclusion of the initial size distribution illustrates evolution of aerosols over the intervening time. Observations are included from two instruments on the G-1: the FIMS (orange) and the PCASP (pink) which, respectfully, resolve the majority of the Aitken and accumulation mode sizes (Section 2.1). In situ values are shown as median (solid) and interquartile range (shading) over the comparison period and can be contrasted with the comparable SAM median (solid).

moves toward the characteristic modal diameter for the accumulation mode, mainly due to chemical processing, with the Hoppel Transfer reducing overall Aitken aerosol number and the depth of the Hoppel minimum.

Aitken transfer also occurs in the Sc layer, as will be examined later in more detail (e.g., Section 3.2), and contributes to the increase in accumulation number in this layer. Comparing with the size distributions available in the transition layer below the Sc (700 m, Figure 4b), it is apparent that the accumulation mode shifts further to the right than observed. This suggests that generation of accumulation mode aerosols in the lower BL also contributes to the large accumulation concentrations in the Sc layer. Note that the observed and simulated distributions in the FT are assisted in their overlap by nudging above the inversion (Figure 4a). While some activation likely occurs in both the Sc and Cu layers, the magnitude of the deviation from observations suggests the simulated transfer is slightly too efficient. This may, in part, reflect the complexity of initializing a rapidly evolving BL (Section 5).

The majority of the median aerosol size distributions over the observation comparison period are within the observed interquartile range. The relative changes in modal location in the layers below the Cu and Sc indicate distinct underlying causes for these shifts away from the initial distributions, which may be exaggerated by the overly active transfer. Processes driving these disparate shifts will be examined in Section 3.2. Overall, however, simulated aerosol partitioning agrees very well with observations across the sampled depth (particularly for Aitken aerosols, Figures 3a and 3b), suggesting these discrepancies do not negatively impact the total BL behavior.

Ctrl cloud microphysical properties are also in good agreement with observations. In-cloud LWC (Figure 3d) is within the observed interquartile range across the BL, with a slightly dryer Cu layer. N_d (Figure 3e) also agrees well with observations. Note that the <1% cloud fraction portion of the profiles above ~1.5 km are from the overshooting Cu tops above the Sc layer (e.g., Figures 2g–2i). There is a significant difference in the lowest observed quantile near ~500 m. This may be associated with sparse sampling of the Cu clouds in this layer, as evident from the large observational uncertainties (Figures 3d and 3e). Overall, however, the good agreement in N_d across the majority of the BL suggests that the net balance between the evolving aerosol sources and sinks generated in *Ctrl* is realistic.

We can assess the simulated aerosol sinks in more detail using vertical precipitation profile comparisons (Figure 5, Section 2.2). More heavily precipitating rain events are defined where precipitation exceeds a conditional threshold ($P \geq 0.1$ mm day^{-1}), allowing us to examine in-rain precipitation flux (a), rain occurrence fraction (b), and total precipitation flux (c) separately. Cloud drop sedimentation is also included in the simulated and observed precipitation rate estimates. *Ctrl* tends to produce a smaller amount of rain but is still within the interquartile range (a). It tends to rain over a similar portion of the BL as observed (b). Total precipitation flux is also within the observed interquartile range throughout the BL (c). Overshooting Cu tops are apparent in the in-rain precipitation flux (a) but not in the total (c) or rain fraction (b), indicating their contribution is very small. In both *Ctrl* and observations, meaningful precipitation peaks at similar heights.

The separation between the mean and median estimates of both in-rain (a) and total precipitation flux (c) suggests that *Ctrl* simulates a more consistently drizzling cloud system than the infrequent but heavily raining system observed during RF16. The mean and median are significantly separated in observations: RF16 sampled a few heavily precipitating clouds (~30 mm day^{-1}) but fewer lightly precipitating clouds (a, c). *Ctrl* has slightly closer mean and median behaviors and a generally lower mean than observed: there are fewer heavily precipitating clouds produced compared to observations but more frequent drizzling clouds producing a median within the observed interquartile range without pushing the mean toward the higher, observed values (a, c).

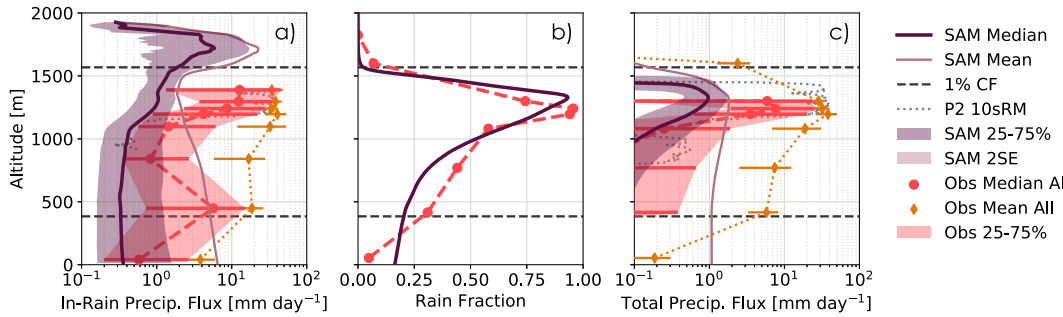

Figure 5. Model-observation vertical profile comparisons for precipitation measures over 12:00–14:30 UTC. Total profiles are computed (as in Figure 3) for: (a) in-rain precipitation flux, (b) rain fraction, and (c) total precipitation flux. Rain is determined based on the conditional threshold, $P \geq 0.1$ mm day^{-1}. In addition to median and interquartile range, means are also shown (diamonds and dotted line for observations, thin line for SAM). The cloud layer edges in SAM, where median cloud fraction is 1%, are included for reference as dark gray, dashed horizontal lines.

Finally, we can evaluate the *Ctrl* radiative properties over the comparison period using satellite observations. In order to capture the spread in cloud behavior across this case when using the coarser satellite data, we utilize 49 samples of comparable size to the simulation domain (0.25° × 0.25°) sampled within a 2° × 2° box overlapping the flight sampling region (Section 2.1). Subdomain means and PDFs indicate the spread in behavior seen in all three satellite retrievals for this region and time (Figure 6). After coarsening the SAM output to the satellite resolution (Figure S2 in Supporting Information S1), we see that the *Ctrl* simulation (purple) tends toward the upper end of the observed behavior for LWP and albedo but matches the mean τ behavior.

Because *Ctrl* N_d corresponds well with in situ observations (Figure 3e), we expected this good agreement in the optical properties. However, this comparison also demonstrates the contribution of column liquid water to overall radiative properties. Despite simulating similar τ as observed, *Ctrl* tends to simulate moister clouds (Figure 6a) and a slightly higher area-mean albedo (c). The tendency toward moister clouds is consistent with the higher LWC (Figure 3d) and higher N_d (e) at the top of the Sc layer and in the overshooting Cu, which was above the aircraft-sampled flight level.

Is the *Ctrl* simulation statistically likely to fall within observed subdomain variability? To test this, we use a PDF constructed from the subdomain means (red) and apply Welch's unequal variances *t*-test to compare the population means of the satellite samples and the simulation. In all cases, the *Ctrl* mean is the same as the satellite subdomain aggregate mean at 95% confidence. The *Ctrl* mean (circle) falls within the 5th–95th range from the

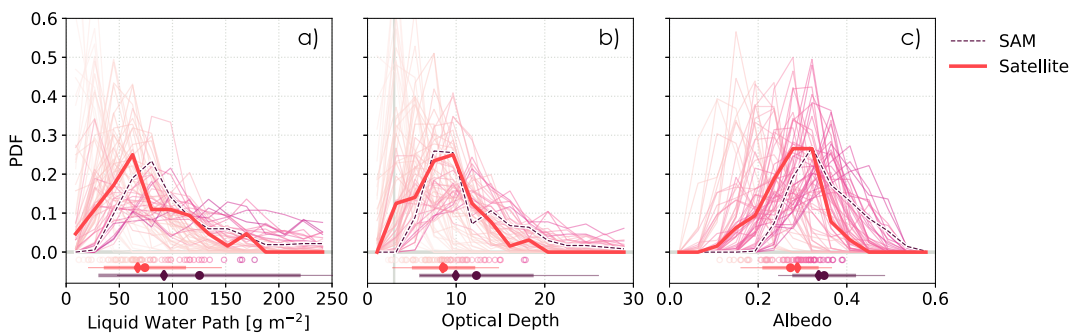

Figure 6. Model-observation comparison for satellite observations over 12:00–14:30 UTC: (a) cloud liquid water path, (b) cloud optical depth, and (c) albedo. PDFs for each satellite subdomain (thin lines, colored by subdomain mean value) are shown along with their means (colored circles). A PDF constructed from the subdomain means (red) is shown along with descriptive statistics: mean (dot), median (diamond), standard deviation (thick line), and 5th–95th range (thin line). A PDF comparable to the subdomain PDFs is constructed from the *Ctrl* simulation coarsened to the satellite resolution (purple, thin dashed line). Model statistics for comparison to the observations are also included. See Section 2.1 for further sampling details. In (b), the optically thin cloud threshold ($\tau = 3$) is shown as a gray line (O, Wood, & Tseng, 2018).

satellite subdomain aggregate (thin line). Thus, the *Ctrl* simulation is consistent with satellite observed cloud property variability despite a small tendency toward moister and brighter observed cloud behaviors.

We conclude that the W22 configuration of SAM with this specified initialization method captures the majority of the key features of the decoupled low cloud regime sampled in RF16. *Ctrl* exhibits skill in generating and maintaining aerosol across the FT and the majority of the BL in both number and size distributions. The main exception is near cloud layers where there are small discrepancies in aerosol partitioning between modes due to Aitken particles being too readily activated and increasing the accumulation mode beyond the observed range. *Ctrl* also tends to produce a cloud with slightly higher liquid water amount and fewer heavily precipitating clouds than observed. Some of the forcings for this case study (i.e., imposed large scale uplift) and necessary initialization choices (i.e., BL moistening of reanalysis to resemble observations) may encourage this macro-physical response. However, neither the small differences from observations in aerosol nor cloud appear to negatively effect N_d or the net balance of aerosol sources and sinks. *Ctrl* produces τ and domain-mean albedo within statistical agreement of satellite observed ranges, suggesting SAM has sufficient skill to accurately analyze radiative property sensitivity to aerosol changes. The small differences between observed and *Ctrl* behaviors will be revisited in Section 5. However, the fidelity of the *Ctrl* simulation in capturing aerosol and aerosol-cloud-precipitation interactions is sufficiently robust to justify further analysis: (a) identifying key aerosol-cloud-precipitation processes in this morphology regime (Section 3.2) and (b) evaluating regime sensitivity to changes in aerosol conditions (Section 4).

3.2. Identifying Key Aerosol-Cloud-Precipitation Processes

Satisfied with the agreement between observations and our constrained aerosol-coupled LES for this case, we can examine the time evolution of aerosol-cloud-precipitation interactions and identify which processes dominate the behavior of this decoupled low cloud regime. Figure 7 shows the vertical, time evolving profile of N_{acc} (a) along with the Aitken transfer tendency (b), updraft strength (i.e., vertical velocity variance, c), and N_{ait} (d). After release at 9:00 UTC, Aitken aerosol is transferred gradually to the accumulation mode in many small Cu-layer updrafts between ∼250–500 m, depleting the initial Aitken aerosol. Sub-cloud layer convection combines with large-scale advective forcing to erode a weak stable layer (evident in Figure S5 of Supporting Information S1) and enables enhanced shallow moist convection and an associated increase in Aitken transfer to accumulation mode after 11:00 UTC (Figures 7b and 7c). As seen in Figure 2, these Cu contribute to transport and mixing between the lower and upper cloud and aerosol layers. After 14:30 UTC, Aitken activation and transfer occurs mostly in the Sc layer updrafts, which become more robust by the end of the simulation (after 16:30 UTC) and appear to be driven by increasing cloud top radiative cooling in the evening hours (not shown). However, N_{acc} does not increase simultaneously, suggesting that this N_{ait} activation is buffering aerosol and droplet number concentrations against precipitation depletion.

To delve further into aerosol processes affecting these two cloud layers and their interchanges, we calculate three atmospheric layer number budgets (Section 2.2, Figure S7 in Supporting Information S1) examining: (a) the total depth, including the BL and lower FT (0–1.6 km, Figure 8a), (b) the upper layer (0.8–1.6 km, Figure 8b), and (c) the lower layer (0–0.8 km, Figure 8c) tendencies. A corresponding mass budget (Figure S8 in Supporting Information S1) is also computed and will be discussed where relevant. Figure 8 presents the mean tendencies of the leading terms (Equation 2) contributing to the Aitken and accumulation number evolution. To aid in interpretation, we focus on the mean tendencies over three reference periods (highlighted in Figure 7d): after release (9:00–12:00), during the observation comparison (12:00–14:30), and when accumulation sources and sinks are in quasi-balance (14:30–21:00 UTC). We also include a summary schematic illustrating these key processes (Figure 9).

Aitken transfer dominates the number tendencies in the total budget for both the Aitken (as a sink) and accumulation modes (as a source). Aitken transfer peaks during the observational comparison period and then decreases over time, with the fewest particles transferred to the accumulation mode during the final period. The removal of accumulation mode aerosol through wet scavenging mirrors these tendencies but with a smaller magnitude. The result is a relatively constant, positive total accumulation number tendency across the BL and throughout the simulation due to the Aitken transfer out competing the wet scavenging accumulation number tendencies ($\dot{N}_{Tot.\,acc} > 0$). Aitken number tends to be lost throughout the simulation and BL ($\dot{N}_{Tot.\,ait} < 0$), peaking in loss the same period that there is the largest transfer (12:00–14:30 UTC).

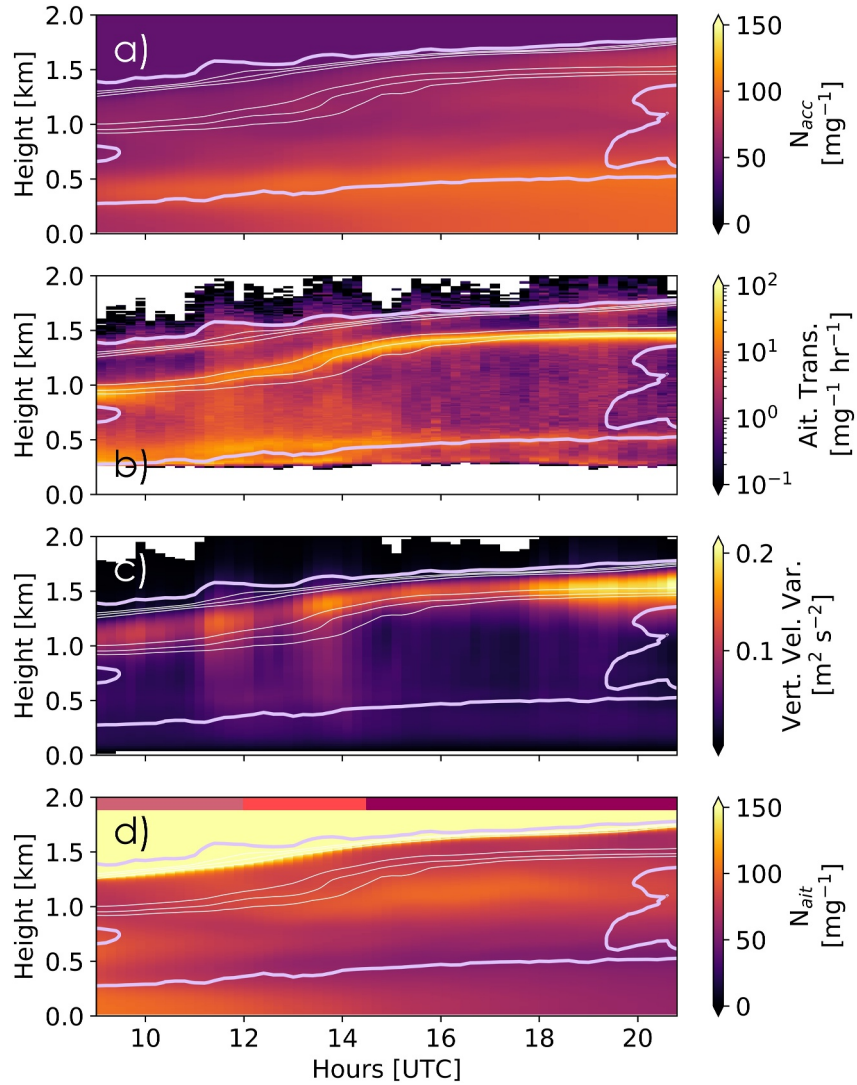

Figure 7. Time versus altitude profiles showing the *Ctrl* evolution of (a) accumulation number concentration (in and out of cloud), (b) Aitken transfer rate, (c) vertical velocity variance, and (d) Aitken number concentration. Contours of 0.05, 0.1, and 0.2 g kg^{-1} liquid water (thin white lines) and 10% cloud cover (thick purple line) are included for reference. Three time periods are marked in (d) for future reference: 9:00–12:00 (pink), 12:00–14:30 (red), and 14:30–21:00 UTC (dark red). Vertical velocity variance <0.003 m^2 s^{-2} and Aitken transfer <1 mg^{-1} day^{-1} are not shown.

In all layers, the mass budget (Figure S8 in Supporting Information S1) is dominated by accumulation mode tendencies. Once activated, chemical processes quickly grow solute mass and diameter, committing the particles irreversibly to the accumulation mode and likely continuing to increase their size over time (e.g., Feingold & Kreidenweis, 2002) with potential assistance from collision-coalescence (e.g., Hoffmann & Feingold, 2023). Mass increases through chemical processing are partly offset by sedimentation removal. Mass is gained throughout the first two periods before the sources and sinks begin to balance during the final period.

Dividing the total budget into layers encapsulating the Cu (lower) and Sc (upper) clouds adds additional nuance to this story. Turbulent and convective fluxes act to mix and redistribute particles between layers. The net flux of Aitken aerosols is downward, from the upper layer (bottom flux) into the lower layer (top flux) partly due to Cu updrafts carrying anomalously small Aitken aerosol concentrations (Figures 2a–2c). Accumulation aerosols are simultaneously fluxed in the opposite direction: exported from the lower layer into the upper layer. Flux tendencies peak in both layers during the 12:00–14:30 UTC period.

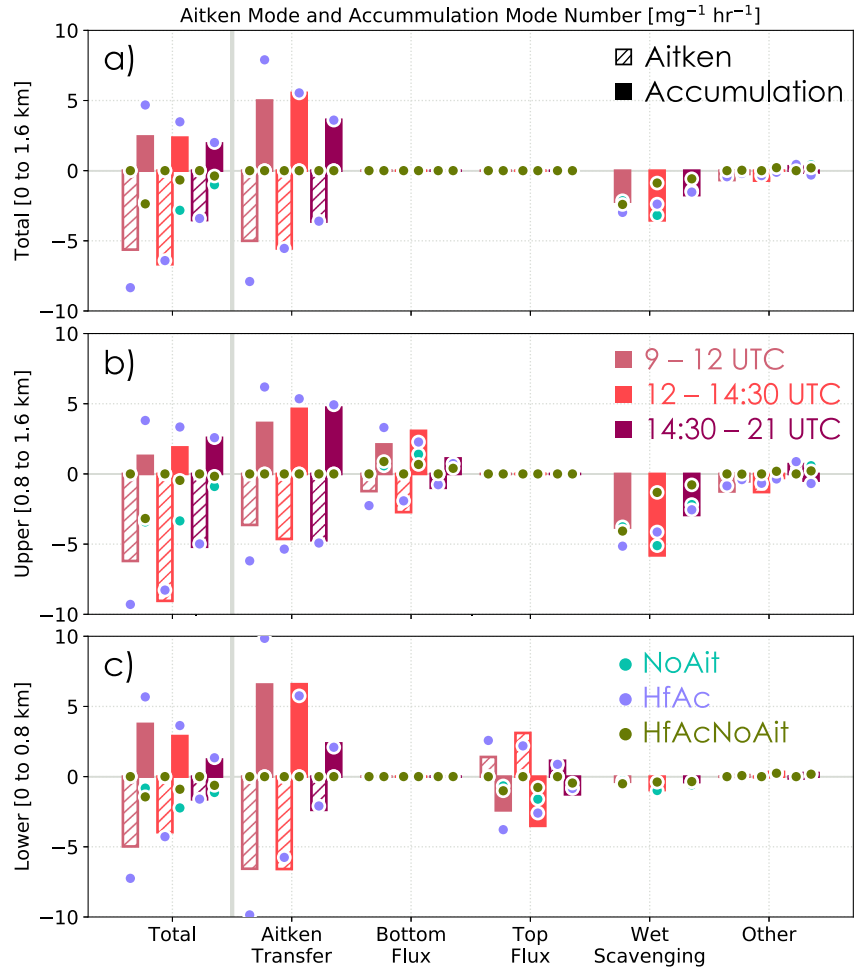

Figure 8. Evolution of leading number budget terms for Aitken (hatched) and accumulation modes (solid bars) computed over the total depth (a, 0–1.6 km), over the upper layer (b, 0.8–1.6 km), and over the lower layer (c, 0–0.8 km). Mean number tendencies are computed for the three time periods (left to right in each term category) highlighted in Figure 7d: 9:00–12:00 (pink), 12:00–14:30 (red), and 14:30–21:00 UTC (dark red). Bars show *Ctrl* mean tendencies while dots show equivalent values for the sensitivity studies (Section 4). Total tendency is to the left of the gray division line and contributions from individual terms are to the right. Companion plots for all number and mass tendency terms versus time for the *Ctrl* and aerosol sensitivity simulations are in Figures S7 and S8 of Supporting Information S1.

Aitken transfer dominates the lower layer, leading to a negative $\dot{N}_{Tot.\ ait}$ and positive $\dot{N}_{Tot.\ acc}$ at all times despite exchanges with the upper layer. Both $\dot{N}_{Tot.\ acc}$ and $\dot{N}_{Tot.\ ait}$ magnitudes decrease with time. This is due to the combined effect of fluxes peaking at 12:00–14:30 and decreasing Aitken transfer tendency during 14:30–21:00 UTC, reducing the amount of aerosols being both generated and brought into the lower layer.

In the upper layer, $\dot{N}_{Tot.\ acc}$ and $\dot{N}_{Tot.\ ait}$ have the same signs as in the lower layer but evolve very differently. $\dot{N}_{Tot.\ acc}$ increases with time while $\dot{N}_{Tot.\ ait}$ has the largest loss at 12:00–14:30 UTC. Wet scavenging is a significant sink of accumulation aerosols in this layer, peaking in the 12:00–14:30 period but unable to overcome the sources of accumulation aerosols. $\dot{N}_{Tot.\ ait}$ peaks in the 12:00–14:30 period, an apparent lag from the lower layer tendencies. This lag between layers is likely due to the delay while Aitken aerosols are transferred in the lower layer and fluxed upwards. It may also be related to entrainment of Aitken aerosols as the BL deepens over time. Local Aitken transfer rates also increase with time in the upper layer, assisting in resisting the precipitation depletion effects on accumulation aerosols.

Note that in-cloud scavenging weakly reduces Aitken in the upper layer (9:00–14:30) and, in the final period, large-scale subsidence of Aitken from the FT weakly increases Aitken number in the upper layer (Figure S7c in

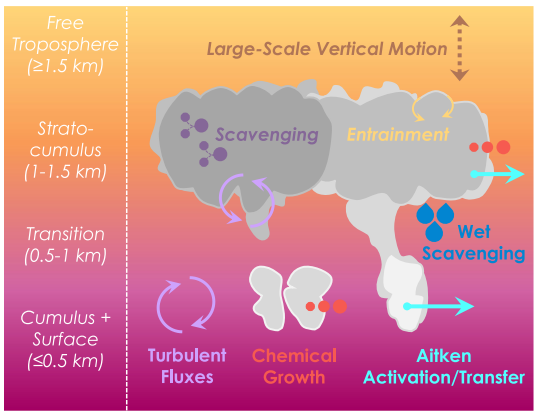

Figure 9. Key aerosol-cloud-precipitation processes involved in the evolution of the morphology regime observed during the RF16 research flight on 15 July 2017. The key terms shown are Aitken activation/transfer (occurring at all cloud layers), turbulent fluxes (eddies moving particles between layers), wet scavenging (aerosol depletion in rain), and mass growth through chemical processing. Scavenging (aerosol depletion in cloud), large-scale vertical motion (including subsidence and ascent, which may encourage cloud moistening and increased organization) and entrainment of aerosols are included for completeness but do not contribute as strongly over this simulation's duration.

Supporting Information S1). A longer entrainment period or a larger FT Aitken concentration would be necessary to restore BL Aitken aerosol (see W22 sensitivity studies, discussion in Section 5). Weak winds lead to insignificant surface aerosol fluxes (Section 2.2, Figures 8a and 8c). In this case, Aitken is lost at all levels and times ($\dot{N}_{Tot.\ ait} < 0$).

To summarize (Figure 9), in this decoupled low cloud regime Aitken mode aerosol is activated into the accumulation mode and grown through chemical processing in both Cu and Sc cloud layers. Turbulent and convective eddies mix Aitken aerosols down from the upper layer into the lower layer where they are transferred to the accumulation mode. Simultaneously, eddies export accumulation particles up into the transition and Sc layers where they are activated into droplets in updrafts. Precipitation depletion through wet scavenging removes accumulation aerosol in Sc (and weakly in Cu), partially off-setting the increase in BL accumulation particles from Aitken transfer. This resistance to precipitation loss and the accompanying maintenance of N_d associated with Aitken activation into the precipitation-depleted accumulation mode is a hallmark of the Aitken-buffering mechanism (McCoy et al., 2021).

4. Sensitivity Studies

In this section, we build on the *Ctrl* simulation with three additional simulations that examine the sensitivity of the RF16 cloud system and its aerosol-cloud-precipitation processes to changes in accumulation and Aitken aerosol number concentrations (Section 2.2, Table S1 in Supporting Information S1). *HfAc* reduces the initial *Ctrl* accumulation number by half throughout the entire profile. It asks whether the amount of Aitken aerosol in *Ctrl* can still buffer the aerosol-cloud-precipitation system against precipitation depletion in a reduced accumulation-mode environment. *NoAit* removes Aitken aerosol throughout the entire initial profile and tests whether Aitken aerosol is important to sustaining the accumulation profile against precipitation depletion. *HfAcNoAit* uses the accumulation profile of *HfAc* and the Aitken profile of *NoAit* to evaluate whether the aerosol and cloud profiles can be sustained against precipitation removal in the reduced accumulation case *without* the help of Aitken aerosol.

Differences between these simulations are immediately apparent from the time series of certain key parameters (Figure 10). Two types of behavior are encapsulated by these simulations: Aitken-buffered (*Ctrl*, *HfAc*) and Aitken-deficient (*NoAit*, *HfAcNoAit*) systems. When Aitken aerosols are present, the Aitken-buffering mechanism helps clouds to maintain coverage (a) despite depletion of LWP (c) through persistent precipitation (b). Aitken aerosol is steadily lost over time in *Ctrl* and *HfAc*, mostly through transfer to the accumulation mode, whose concentration increases steadily throughout these two simulations (e) (from ∼50 to ∼70 mg^{-1} in *Ctrl*, and ∼25–55 mg^{-1} in *HfAc*). In contrast, the Aitken-deficient simulations (*NoAit*, *HfAcNoAit*) have significantly different cloud fraction evolution, beginning to break up at ∼12:00 and 10:00 UTC respectively (a). They steadily lose accumulation aerosols (e) due to precipitation depletion (b, particularly strong in *HfAcNoAit*) that is uncompensated by Aitken transfer. The trend in accumulation mode for all simulations is reflected by N_d in the upper Sc and lower Cu cloud layers (Figure 10f).

Snapshots at 14:00 UTC (Figure 11) highlight the differences in aerosol and cloud morphology across the simulations. Compared to *Ctrl*, all studies exhibit more separated upper level mesoscale cells generated from Cu rising into Sc with a larger proportion of intervening optically thin cloud layers. *HfAc* maintains cells very similar to those in *Ctrl*, albeit with smaller convective structures and slightly lower τ across the domain. Clouds in the Aitken-deficient cases are much more heterogeneous than in the Aitken-buffered cases. *NoAit* has much smaller and more broken cells with a much reduced cloud cover and lower τ. The Sc in *HfAcNoAit* has already collapsed by 14:00 UTC, leaving the BL dominated by broken cumuliform structures with a few optically thin layers remaining from precipitation-depleted clouds.

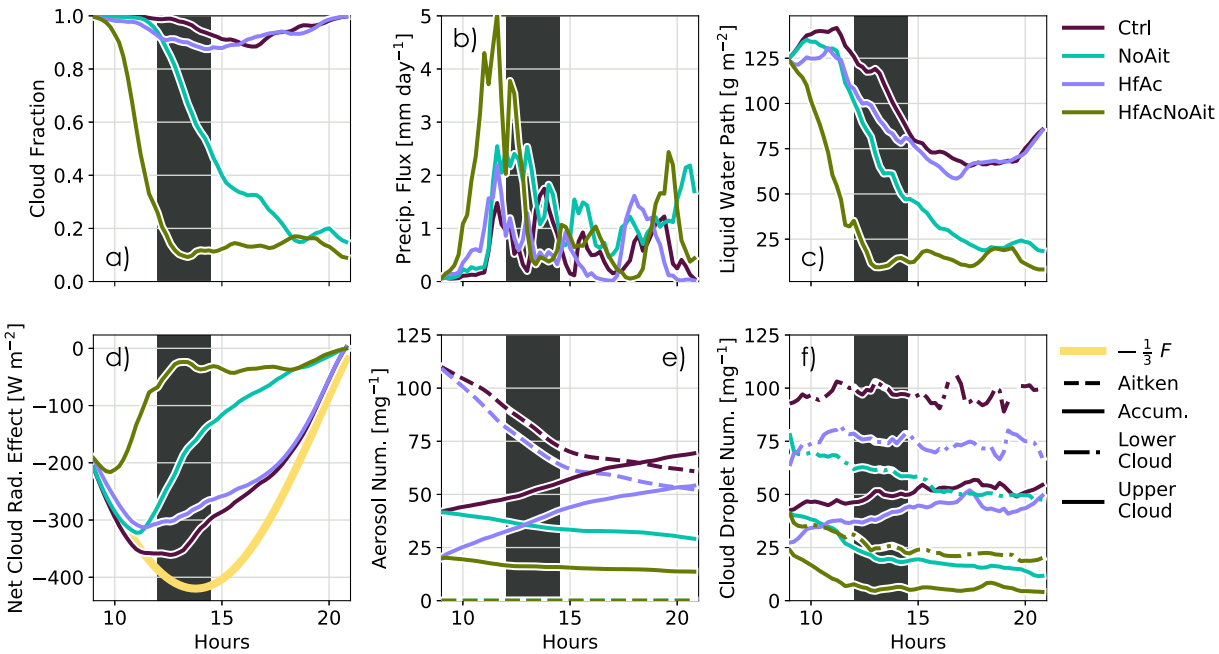

Figure 10. Time evolution of key SAM parameters for *Ctrl*, *HfAc*, *NoAit*, and *HfAcNoAit* simulations: (a) cloud fraction, (b) precipitation flux at the surface, (c) liquid water path, (d) net cloud radiative effect, (e) Aitken (dashed) and accumulation (solid) aerosol number concentrations (≤1.6 km), and (f) mean droplet number concentration in the upper, Sc (≥0.8 km, solid) and lower, Cu (≤0.8 km, dash dot) cloud layers. Observation comparison period shown in dark gray (12:00–14:30 UTC). Top of atmosphere incoming solar radiation (F, W m^{-2}) scaled by $-\frac{1}{3}$ is included on (d) for diurnal cycle reference.

Notably, the Aitken-buffered *HfAc* case loses less N_d, LWP, cloud amount, and NetCRE compared to the Aitken-deficient *NoAit*. The reason for this is apparent from Figure 10e: Aitken transfer restores the halved accumulation number to the initial *Ctrl* levels by 14:30 UTC, forestalling further precipitation depletion as N_{acc} continues to be enhanced. Ultimately, the total aerosol number is what matters for the system, which is why the Aitken-buffering

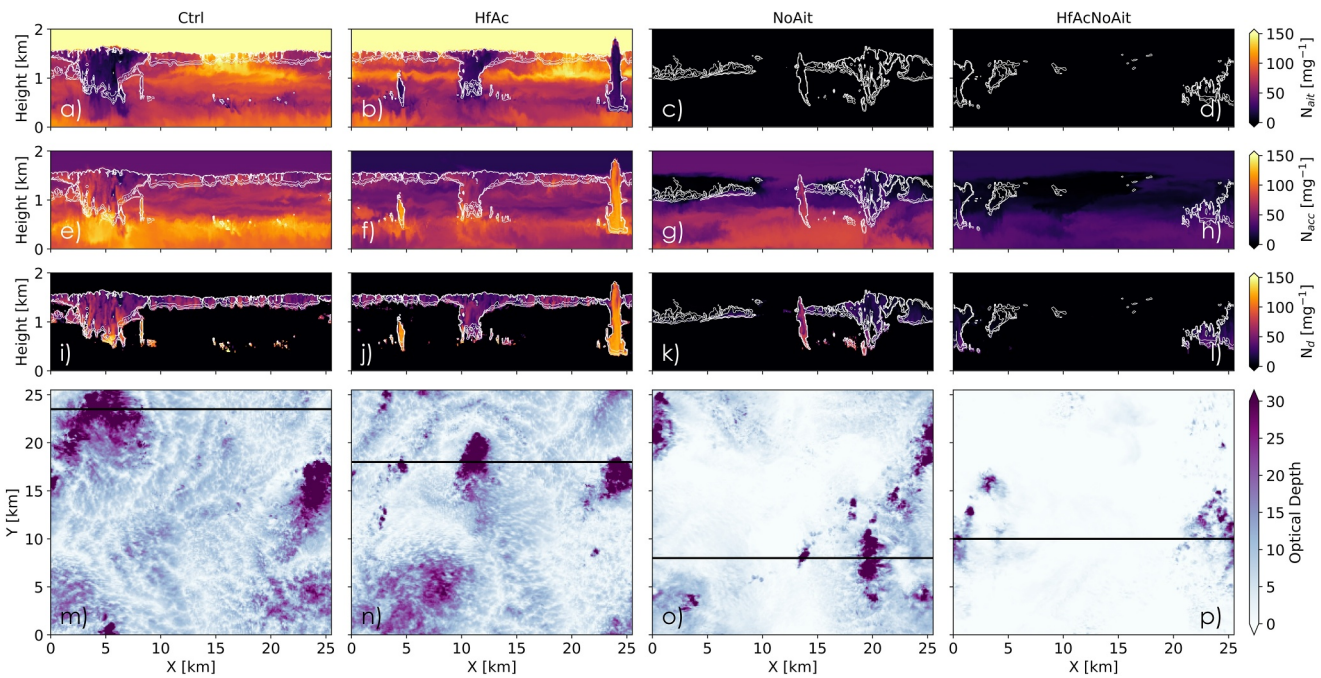

Figure 11. Cross sections of SAM sensitivity studies at 14:00 UTC as in Figure 2: *Ctrl* (a, e, i, m), *HfAc* (b, f, j, n), *NoAit* (c, g, k, o), and *HfAcNoAit* (d, h, l, p). Parameters shown are Aitken (a–d), accumulation (e–h), and cloud droplet (i–l) number concentrations and cloud optical depth (m–p).

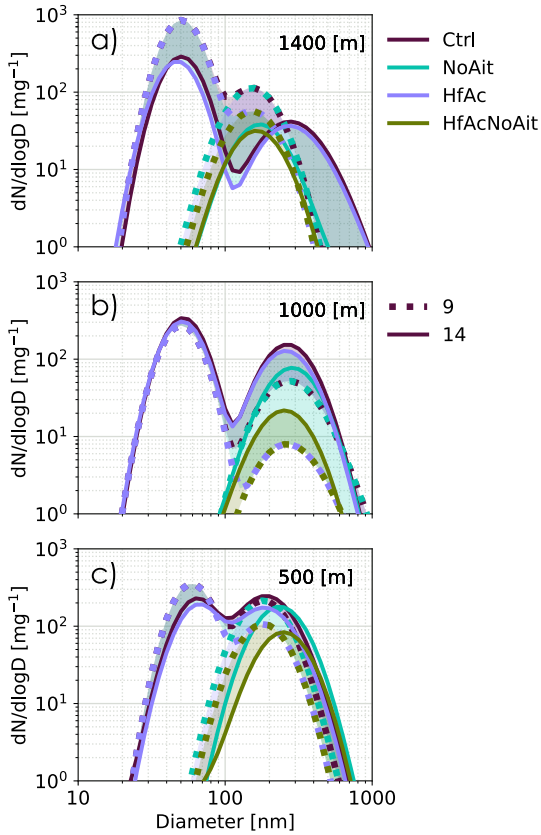

Figure 12. SAM size distributions evolving (shading) from 9:00 (dotted) to 14:00 UTC (solid line) for sensitivity studies: *Ctrl*, *HfAc*, *NoAit*, and *HfAcNoAit*. Distributions are shown at three levels: (a) the FT (9:00 UTC) that the Sc cloud layer grows into (14:00 UTC, 1.4 km), (b) the Sc cloud base (9:00 UTC) and, later, Cu columns (14:00 UTC, 1 km), and (c) the lower Cu cloud layer (9:00 UTC) and later base of Cu columns (14:00 UTC, 0.5 km).

mechanism is effective. Access to Aitken aerosol in *HfAc* is a larger deterrent against precipitation depletion of N_{acc} and N_d than larger initial values of N_{acc} and N_d in *NoAit*. This is taken to the extreme in *HfAcNoAit*, where accumulation number is halved and the sustaining Aitken influence is removed. Without Aitken aerosol to restore accumulation aerosol, the *HfAcNoAit* cloud system cannot resist precipitation depletion and has the largest loss signatures of all the simulations.

For all cases, N_d is higher in the Cu than the Sc layers. This is not unexpected based on the initially larger net gain in Cu accumulation aerosols compared to the Sc layer, as seen in the *Ctrl* budgets and in varying degrees across the sensitivity studies (Figure 8c and Figure S7e in Supporting Information S1). We can examine the sensitivity study tendencies in more detail by contrasting their budget results (dots in Figure 8) and size distribution evolution (Figure 12).

In general, *HfAc* budgets behave the same as the *Ctrl*. However, it has a much larger initial Aitken transfer and stronger fluxes (9:00–12:00 UTC in Figure 8), which is consistent with the system compensating for the smaller initial accumulation number, as discussed previously. Aitken tendencies return to similar levels as *Ctrl* in subsequent periods, but $\dot{N}_{Tot.\,acc}$ is slightly larger than *Ctrl* during 12:00–14:30 UTC thanks to weaker wet scavenging and fluxes. The size distribution evolution in the Sc layer has similar tendencies for *Ctrl* and *HfAc* over 9:00–14:00 UTC (Figures 12a and 12b). As the Sc layer (a, 1.4 km) grows into the FT (Figure S9a in Supporting Information S1), the Aitken mode is depleted and the accumulation mode shifts strongly to the right, creating a well defined Hoppel minimum associated with cloud (e.g., Hoffmann & Feingold, 2023) and chemistry processing. Aitken is transferred similarly in *Ctrl* and *HfAc*, reducing the Aitken number in both and marginally shifting the mode left in *HfAc*. The matching evolution in their accumulation modes suggests the larger *Ctrl* wet scavenging depletes its larger initial N_{acc}, bringing it in line with *HfAc*.

Near the bottom of the Sc layer (b, 1 km), which subsequently experiences rising Cu towers, the accumulation mode grows more in *HfAc* than *Ctrl* such that their distribution matches at 14:00 UTC. *HfAc*'s evolution is likely assisted by stronger fluxes of accumulation aerosols from the transition layer (Figures 8b and 8c). A rightward shift of the accumulation mode, and depletion of Aitken, happens in the transition layer for both *HfAc* and *Ctrl* (Figure S9b in Supporting Information S1). This is consistent with augmentation of accumulation through Aitken transfer and fluxes from the Cu layer as well as modal shifts due to increasing mass by chemical processing.

In the Cu layer (Figure 12c), Aitken aerosols are transferred locally to the accumulation mode, reducing the Aitken number. Again, chemical processing shifts modes to the right such that the two distinct, initial aerosol modes are brought together, reducing the Hoppel minimum. Stronger *HfAc* turbulent fluxes export accumulation particles, likely helping to redistribute particles between layers and maintain the accumulation mode. The *HfAc* budget and distribution tendencies are confirmation of both where the largest transfer occurs in the system (in the cloud layers before turbulent fluxes redistribute particles) and how the transfer and fluxes readjust in order to restore depleted accumulation aerosol and buffer the cloud system.

Under Aitken-deficient conditions (*NoAit*, *HfAcNoAit*), precipitation depletion leads to a loss of accumulation number at all levels (Figure 8). Turbulent fluxes still move accumulation number from the Cu to the Sc layer but the import of accumulation number is insufficient to offset removal through wet scavenging in the Sc. N_d decays at a similar rate in the Cu and Sc layers (Figure 10f) as a result of precipitation-driven cloud breakup (dominating the Sc layer) and accumulation export through turbulent fluxes (dominating the Cu layer) in the absence of restorative Aitken aerosols. Over 9:00–14:00 UTC, the accumulation mode (Figure 12) shrinks at the top of the Sc layer (a) and grows at its base (b) under the influence of precipitation depletion (dominating a) and flux transport.

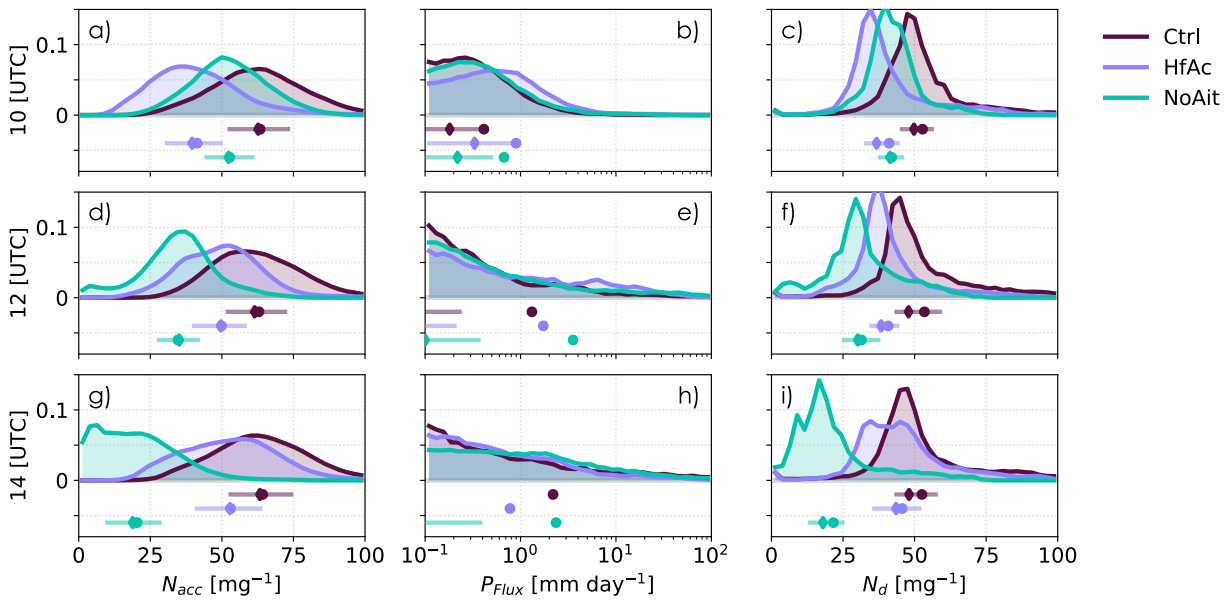

Figure 13. PDFs at native model resolution for the *Ctrl*, *HfAc*, and *NoAit* simulations at (a–c) 10:00, (d–f) 12:00, and (g–i) 14:00 UTC. N_{acc} (a, d, g) and N_d (c, f, i) are for all values in the upper cloud layer (≥0.8 km) while precipitation flux (b, e, h) is through the bottom edge (0.8 km).

Fluxes are weaker in these simulations, helping to grow the accumulation mode in the Sc layer before depletion (b, Figure S9b in Supporting Information S1) but fluxing fewer accumulation aerosols from the Cu (c) and sub-cloud layers (Figures S9b and S9c in Supporting Information S1). Chemical processing is still a significant influence on the accumulation mode before too many aerosols are lost (Figure S8 in Supporting Information S1), contributing to the small modal shift near the Sc (Figure 12a and Figure S9b in Supporting Information S1) and Cu (Figure 12c and Figure S9c in Supporting Information S1) layers. The *NoAit* and *HfAcNoAit* tendencies confirm that without Aitken aerosols, the cloud system undergoes a more rapid collapse driven by both precipitation depletion (even larger in *HfAcNoAit*, Figure 10b) and redistribution of particles through turbulent fluxes helping to accelerate collapse rather than resupplying new accumulation aerosols as in the Aitken-buffered system.

The impact of Aitken buffering on radiation is seen in the diurnally varying net cloud radiative effect (NetCRE) (Figure 10d). *HfAc* produces a similar albeit marginally weaker radiative response than *Ctrl*. In contrast, NetCRE for *NoAit* and *HfAcNoAit* are considerably smaller in magnitude with shapes dictated by their cloud break-up (a). *NoAit* and *HfAcNoAit* NetCRE peak just before precipitation flux substantially increases (b) and dissipates their cloud layers (a, c, f).

We can examine this radiative evolution, and its contributing factors, in more detail with time evolving PDFs of key variables over 10:00–14:00 UTC (Figures 13 and 14). Because the *HfAcNoAit* simulation is already fairly collapsed at 12:00 UTC, we focus on contrasting the still evolving simulation behaviors of the *Ctrl* with *NoAit* and *HfAc* over this period. Figure 13 highlights the aerosol-cloud-precipitation evolution we expect from these three sensitivity studies (e.g., Figures 8 and 10). While precipitation increases over time (b, e, h), *HfAc* N_{acc} (a, d, g) and N_d (c, f, i) PDFs shift toward *Ctrl* PDFs as Aitken aerosols transfer to the accumulation mode and, despite their initial decrease, restore N_{acc}, N_d back toward the unperturbed *Ctrl* simulation. By 14:00 UTC, the mean and median of N_{acc}, N_d for *HfAc* have been buffered to within the interquartile range of *Ctrl*. In contrast, *NoAit* PDFs for N_{acc}, N_d shift to the left, away from the *Ctrl*, in response to increasing precipitation depletion in the absence of Aitken buffering. Thus, Aitken aerosol presence is critical for sustaining N_d in the *Ctrl*, *HfAc* simulations, as evidenced by the swap in PDF location between *NoAit* and *HfAc* by 14:00 UTC.

Aerosol behavior controls the ability to sustain cloud homogeneity (Figure 11) and NetCRE (Figure 14). One can also measure the inverse of this, or the amount of optically thin cloud layers (larger percentage with $\tau \leq 3$, Figures 14b, 14e, and 14h). There are far more of these generated in the *NoAit* case by 14:00 UTC compared to *Ctrl* and *HfAc*, consistent with the more visually heterogeneous clouds of that simulation (Figures 11c, 11g, 11k, and 11o). It is also worth noting that the increasing magnitude and PDF broadening that occurs for NetCRE

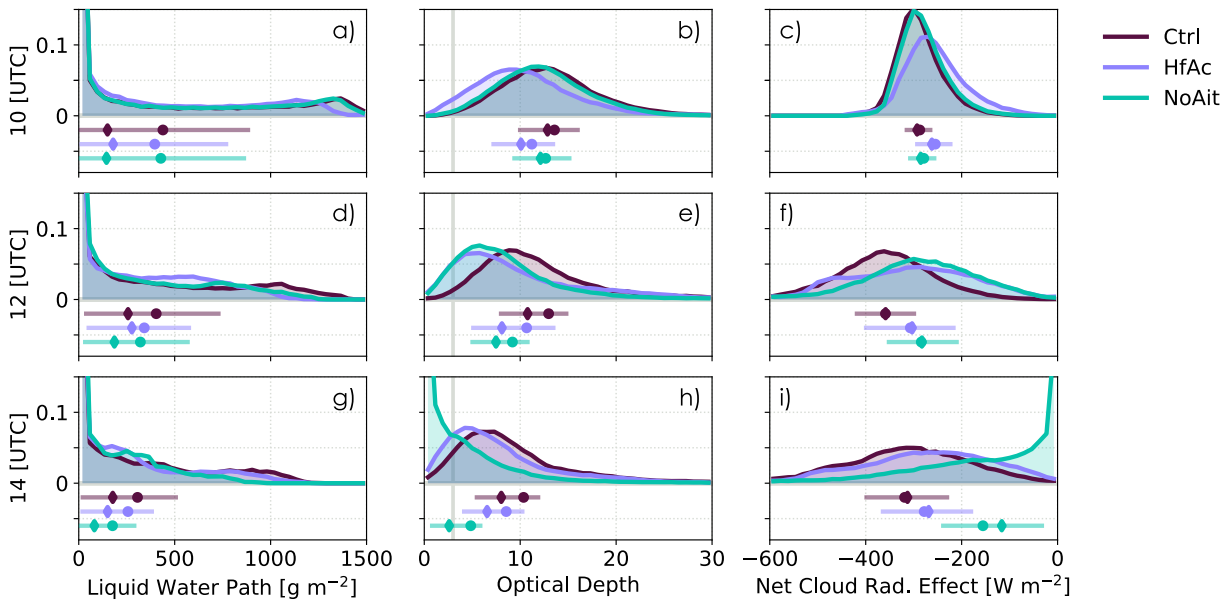

Figure 14. As in Figure 13 but for the: liquid water path in the upper Sc layer (a, d, g, for ≥0.8 km), cloud optical depth (b, e, h), and net cloud radiative effect (c, f, i). A gray line in (b, e, h) references the optical depth threshold ($\tau = 3$) for optically thin clouds (O, Wood, & Tseng, 2018).

happens at the same time that the LWP decreases in *Ctrl*, *HfAc* (Figures 14f and 14i). Generally, the time of largest wet scavenging (12:00–14:30 UTC, Figure S7 in Supporting Information S1) occurs when large-scale ascent is peaking (12:00–15:00 UTC, Figure S3 in Supporting Information S1). This suggests that the influence of large-scale meteorology and aerosol processing are fundamentally linked, an important topic for future investigations.

5. Discussion

5.1. Buffering Timescales

In this decoupled Cu rising into Sc case, processes influencing cloud and aerosol evolution operate over hours. Rapid aerosol evolution is driven by Aitken activation, turbulence, precipitation depletion, and chemical processing (Figure 9). Precipitation loss begins to impact accumulation number and mass almost immediately in the *Ctrl* simulation (Figures 8 and 10). The system is still buffered against cloud break-up, however, as depletion is prevented by Aitken transfer and turbulent fluxes throughout the simulation (Figure 8).

The role of the elevated FT Aitken concentrations in the maintenance of BL cloud and aerosols is worth exploring in this case study. Peaks in Aitken concentration near cloud top (e.g., Figures 2b and 2c) and in Aitken transfer profiles (Figure 7b) as well as the Aitken mode depletion and accumulation mode growth at Sc top (Figure 12a) indicate that entrained Aitken aerosol can directly buffer precipitation-depleted clouds (i.e., CCN-depleted supersaturated updrafts may be sufficient to activate locally entrained Aitken particles at cloud top).

The W22 10-day simulations found that large sources of Aitken particles, either from FT import (FT Aitken set to 1,000 mg^{-1}) or surface production (10× surface source) could prevent BL cloud collapse in a subtropical, meteorologically quiescent regime. Our *Ctrl* simulation, particularly the exponential Aitken number depletion signature (Figure 10d), resembles the W22 *BL1000* sensitivity study where BL Aitken concentrations were set to 1,000 mg^{-1} while FT and surface sources were kept small. Cloud breakup was delayed in *BL1000* for twice as long as the control (8 vs. 4 days), suggesting that cloud breakup will be delayed in our case too, even without large FT or surface Aitken sources. Our initial BL Aitken aerosol (∼100 mg^{-1}, averaged over surface and transition values from the initial Aitken profile, Table S1 in Supporting Information S1) was either brought in from the FT over the past few days, generated from sea spray production (Lawler et al., 2021; Xu et al., 2022), or formed via new particle formation in the ultra-clean outflow at cloud edges (Kazil et al., 2011) or within the BL (Zheng et al., 2021). Since our model neglects the new particle production mechanism and has a very small surface source of Aitken aerosols in this weak-wind case, it is best used to quantify FT influence.

Using a marine BL mass weighted average, we estimate that ∼60 mg^{-1} of Aitken mode aerosol particles were transferred to the accumulation mode over the full duration of the *Ctrl* simulation (9:00–21:00 UTC). This represents more than half the initial Aitken value within the BL. The *HfAc* simulation experiences an even larger transfer, ∼70 mg^{-1} from 9:00 to 21:00 UTC. We estimate the entrainment flux of aerosols, determining whether FT entrainment is able to balance these losses and, if not, how many days worth of FT Aitken entrainment are consumed during this event. Our aerosol entrainment source calculation is based on an estimation of the entrainment rate and the jump of aerosols across the inversion (Text S1 in Supporting Information S1). Entrainment from the FT increases Aitken aerosol in the BL by ∼55 mg^{-1} in *Ctrl* and ∼50 mg^{-1} in *HfAc* over 9:00–21:00 UTC. Aitken transfer consumes approximately the same amount of Aitken aerosols as are entrained over the full 12 hr simulation in *Ctrl* (∼0.5 days of FT Aitken entrainment) and ∼1.4× in *HfAc* (∼0.7 days). Note that a similar accumulation mode estimation shows FT entrainment very weakly dilutes BL accumulation concentrations (∼− 5 mg^{-1} lost over 9:00–21:00 UTC in *Ctrl* and ∼ − 10 mg^{-1} in *HfAc*). This is consistent, albeit much smaller in magnitude, with FT accumulation dilution found in similar cloud structures in marine cold air outbreak outflows (Tornow et al., 2022). However, Arctic FT entrainment of Aitken (Igel et al., 2017; Price et al., 2023) and accumulation aerosols (Sterzinger & Igel, 2024) can sustain clouds despite no surface sources and under low BL concentrations, pointing to the complex variation in aerosol influence across cloud regimes.

One can imagine that an air mass might experience increasing Aitken aerosol concentrations during non-precipitating periods which might be consumed during periods of stronger forcing and precipitation. In this way, Aitken buffering of marine BL clouds may be accomplished, in part, with pre-existing Aitken mode aerosols that were entrained from the FT in the preceding days, which may help cases like ours. However, we also note that, at this latitude, the FT Aitken number is observed to have concentrations of ∼210 cm^{-3} with accumulation number concentrations of ∼250 cm^{-3} (Heintzenberg et al., 2000) suggesting there is an additional source of Aitken aerosols that assists in balancing this BL sink (e.g., new particle formation, Zheng et al., 2021).

Expanding on this idea, we note that the above estimation assumes FT Aitken import only occurs locally, neglecting the substantial particle import that occurs with the passage of mid-latitude cyclones (e.g., Covert et al., 1996). Zheng et al. (2021) estimate that in post-frontal open cellular clouds occurring in the ACE-ENA region, which are most likely to experience FT import after the passage of a cyclone, it takes 30–45 hr for FT air to replace the air in a 2 km deep BL. Assuming that the FT concentration of our initial profile (∼250 mg^{-1}, similar to Heintzenberg et al. (2000)) is somewhat representative over this region for this season, we estimate a post frontal entrainment rate of 130–200 mg^{-1} day^{-1} which is, respectively, a factor of ∼1 to 1.7× greater than the Aitken transfer rate during our case (∼−120 mg^{-1} day^{-1}). Aitken transfer during our *Ctrl* case would consume ∼0.3–0.5 days of Aitken aerosol entrained under post frontal conditions. This, even excluding new particle formation at cloud edges (e.g., Kazil et al., 2011) or in the BL (e.g., Zheng et al., 2020), emphasizes that Aitken aerosol can be frequently replenished and that Aitken buffering is likely to be both feasible and important in this region.

5.2. Challenges of Simulating Real-World Case Studies

We encountered a few challenges in simulating this case, in part due to a unique combination of factors. First, the detailed aerosol-cloud-precipitation observations for this morphology regime were taken over a relatively short time period. Second, this regime was rapidly evolving, in part due to the non-trivial meteorological forcing experienced throughout. This made using observations to both initialize and interrogate our simulation complicated, which leads us to an important question about our model construction and its limitations: is our initialization appropriate?

Aitken transfer occurs even in the spinup period of our simulation (e.g., Figure S5 in Supporting Information S1), contributing to the slight mis-partitioning of Aitken aerosol into the accumulation mode near cloud layers compared to observations (Figures 3a and 3b). We found that this behavior was sensitive to the nudging methodology utilized and were able to reduce this issue greatly with the current setup by allowing subcloud turbulence and convection to develop during the spinup period when the spuriously large Aitken transfer associated with the initiation of the cumulus layer could be offset by nudging. As a result, relatively weak transients occur after nudging is switched off, and model-observation aerosol discrepancies are largely restricted to the accumulation mode. Comparisons with satellite observations further benefited from the development of mesoscale organization during the spinup period. Another approach would be to follow Neggers et al. (2019) who select initial values

using a technique that could be successful in our case. They initialize many short-duration, Lagrangian simulations with varying initial states upwind of an observation platform and select conditions producing the smallest biases.

We expect that a more carefully tuned initialization method would have a minor impact on our results, however, and the main improvement would be in reducing the small model-observation aerosol biases in the lower and upper BL. Model-observation consistency elsewhere and for other parameters (especially N_d and the net balance between aerosol sources and sinks) suggests that the model is credible and has skill. Thus, we expect the key mechanisms driving aerosol-cloud-precipitation evolution in this regime and their sensitivity to large changes in the initial aerosol profile (i.e., no Aitken, halved accumulation) are robust.

Our results provide additional (e.g., McCoy et al., 2021) guidance for future observational investigations into Aitken buffering. Aitken activation will be more likely to occur during periods of peak precipitation in the diurnal cycle, when precipitation helps to remove larger aerosols and increase peak updraft supersaturations. Cloud regimes with decoupled boundary layers that include more developed, broken clouds and synoptic or meso-scale ascent are also likely to have more favorable updraft characteristics. Changes in maximum supersaturation deduced from the Hoppel diameter in cloud-free air (e.g., Gong et al., 2023), trends in Aitken or total aerosol number concentrations (e.g., McCoy et al., 2021), cloud droplet number concentration relationships with size-resolved aerosol concentrations (e.g., McCoy et al., 2021) and supersaturations (e.g., Sanchez et al., 2021), and re-sampling of air masses over multiple timescales (e.g., B. Albrecht et al., 2019; Mohrmann et al., 2019) are some methods that would help to identify occurrences of Aitken activation and buffering. As demonstrated by the ACE-ENA instrumental suite (J. Wang et al., 2017, 2022), observations of the full aerosol size distribution, from the Aitken through to the coarse mode, along with cloud and precipitation measurements are critical for any such investigation.

6. Summary

We utilize the System for Atmospheric Modeling (SAM) large eddy scale (LES) model with a novel Aitken-mode enabled microphysics scheme (Wyant et al., 2022, hereafter W22) to investigate a summertime mid-latitude decoupled low cloud regime observed during the ACE-ENA flight campaign (J. Wang et al., 2022). On 15 July 2017, the G-1 aircraft sampled an evolving cloud system composed of cumulus (Cu) rising into stratocumulus (Sc) under heightened Aitken aerosol concentrations (100–200 mg^{-1}) (Figure 1). In situ aircraft observations, reanalysis and satellite retrievals were used to develop and evaluate our case study.

We examined whether a large concentration of BL Aitken aerosols impacted the evolution, radiative properties, and heterogeneity of this cloud system. Using observations to constrain our case study as well as realistic meteorological forcing, we found that the W22 aerosol-coupled SAM captured key time-evolving processes driving BL cloud and aerosol evolution. Profiles of total aerosol number matched observed evolution throughout the BL depth. Aerosols tended to be slightly over-partitioned into the accumulation mode in the cloud layers due to too many Aitken particles being transferred into the accumulation mode in supersaturated updrafts, but were within the observed interquartile range elsewhere. Simulated cloud liquid water was also within the upper end of the observed range, leading to slightly brighter clouds with reasonable optical thickness relative to satellite retrievals. SAM simulated more light precipitation than observed, likely due to aircraft sampling being dominated by a few heavily precipitating clouds. SAM cloud droplet number concentrations matched observations, indicating the minor aerosol and microphysical discrepancies did not ultimately skew the net balance of cloud condensation nuclei (CCN) sources and sinks.

We identified the key aerosol-cloud-precipitation processes driving the evolution of this morphology regime (Figure 9). Aitken activation in the Cu and Sc layers generates accumulation aerosols that are grown by chemical processing throughout the BL. These accumulation aerosols are carried up from the Cu layer to the drizzling Sc layer by turbulent and convective motions. Simultaneously, eddies bring Aitken aerosols down from the transition layer below the Sc to the Cu layer where they can be activated and grown. The continuous transfer of Aitken aerosol to the accumulation mode via activation in cloud droplets in the Cu and Sc layers buffers CCN against precipitation loss. Entrainment of Aitken aerosol from the FT roughly balances the consumption of Aitken aerosols by transfer to the accumulation mode in this case. However, given stronger forcing, precipitation, and wet scavenging, the reserves of Aitken aerosols might be depleted, requiring entrainment of FT Aitken aerosols to

replenish those in the BL. In particular, we estimate that BL Aitken concentrations can be restored between 0.3 and 0.5 days depending on their environment.

Aerosol sensitivity studies illustrate that Aitken buffering is essential in maintaining more homogeneous clouds and preventing their break-up over the 12-hr duration of our simulation. Precipitation-driven break up can be delayed if BL Aitken is present, even under halved accumulation concentrations. Even with the significant meteorological forcings present in the mid-latitudes, the processes driving cloud morphology evolution, heterogeneity, and radiative properties are sensitive to Aitken aerosols. Maintaining more reflective clouds for longer in this environment can be facilitated through Aitken buffering. Accounting for this influence in these pristine environments will be important for reducing aerosol-cloud interaction uncertainty in climate sensitivity.

Appendix A: Sensitivity of Aitken Activation to Simulation Design

We design two studies to test the sensitivity of the *Ctrl* simulation to the formulation of the W22 Hoppel Transfer Scheme. Specifically, we focus on adjusting how the Aitken aerosol is transferred to the accumulation mode and the influence that has on the size of the aerosol that is transferred. In *AltHopV1*, we apply the W22 scheme but transfer mass as an average of aerosols with the critical diameter, D_c, and the integrated mass of the Aitken distribution with $D > D_c$. With this approach, the characteristic diameter of transferred aerosols is larger than in W22, where all transferred aerosols are assumed to have $D = D_c$. In addition, we require that the Hoppel transfer will never make the Aitken modal diameter larger by enforcing:

$$M_{transfer} \geq N_{transfer} \times \left(\frac{M_{Aitken}}{N_{Aitken}}\right) \tag{A1}$$

Rarely, the Aitken mode can be larger than the accumulation mode so that the D_c is smaller than the Aitken modal diameter. In *AltHopV2*, activated Aitken aerosols (i.e., those with $D > D_c$) are transferred only if $D_c < D_{Hoppel}$. The mean size of transferred aerosol increases monotonically from the W22 Hoppel transfer to *AltHopV1* to *AltHopV2*.

We contrast the *AltHopV* studies with the *Ctrl*, *Ctrl LD*, and *NoAit* studies. The *AltHopV* simulations are bracketed by the W22 scheme as originally published (*Ctrl*) and the opposite extreme where no Aitken are allowed to transfer (*NoAit*). In our microphysics scheme, the *NoAit* simulation is the closest possible equivalence to preventing Aitken transfer because activated Aitken aerosols do not exist as a separate category from activated accumulation mode aerosols. We additionally include the *Ctrl LD* study, where the domain has been doubled to 51.2×51.2 km^2, to evaluate the relative influence that the domain size has on the *Ctrl* simulation. We use three time evolution frameworks for our comparisons: mean behavior (Figure A1, like Figure 10), size distributions (Figure S10 in Supporting Information S1, like Figure 12 and Figure S9 in Supporting Information S1) and PDFs (Figures S11 and S12 in Supporting Information S1, like Figures 13 and 14).

Ctrl LD behaves very similarly to the *Ctrl* and is well separated from the extreme *NoAit* simulation. Compared to *Ctrl*, *Ctrl LD* tends to have slightly more cloud breakup before recovery (Figure A1a) and initially more persistent but less prolonged precipitation (b) resulting in a larger eventual depletion in LWP (c) and NetCRE (d). Between 10:00 and 14:00 UTC, *Ctrl LD* is the same as *Ctrl* except for slightly higher LWP prior to the previously noted depletion (Figures S11a, S11d, and S11g in Supporting Information S1). Notably, the accumulation, Aitken, and N_d concentrations match the *Ctrl* behaviors. *Ctrl LD* size distribution evolution matches the *Ctrl* as well except for a small shift to larger accumulation mode particles at the top of the Sc layer (Figure S10b in Supporting Information S1). We conclude that our Aitken buffering results are not sensitive to domain size. The domain size used for the *Ctrl* and all other sensitivity studies is sufficient to capture the characteristics of the mesoscale structures examined in this case (which are smaller than the domain, e.g., Figure 2).

Similarly, the small variations in behavior from the *AltHopV* studies cluster around the *Ctrl* and never present differences as large as between the *Ctrl* and *NoAit* simulations. *AltHopV1* behaves more like the *Ctrl* while *AltHopV2* is slightly more separated. This is consistent with the expectation that the transfer is slowed more in *AltHopV2* than *AltHopV1* relative to the *Ctrl* as the transferred particle size increases. Accordingly, the accumulation mode shifts to larger sizes for *AltHopV1* and, more so, *AltHopV2*. The *AltHopV* Aitken and accumulation modes are slightly more separated over time compared to the *Ctrl*, with a more clearly defined Hoppel

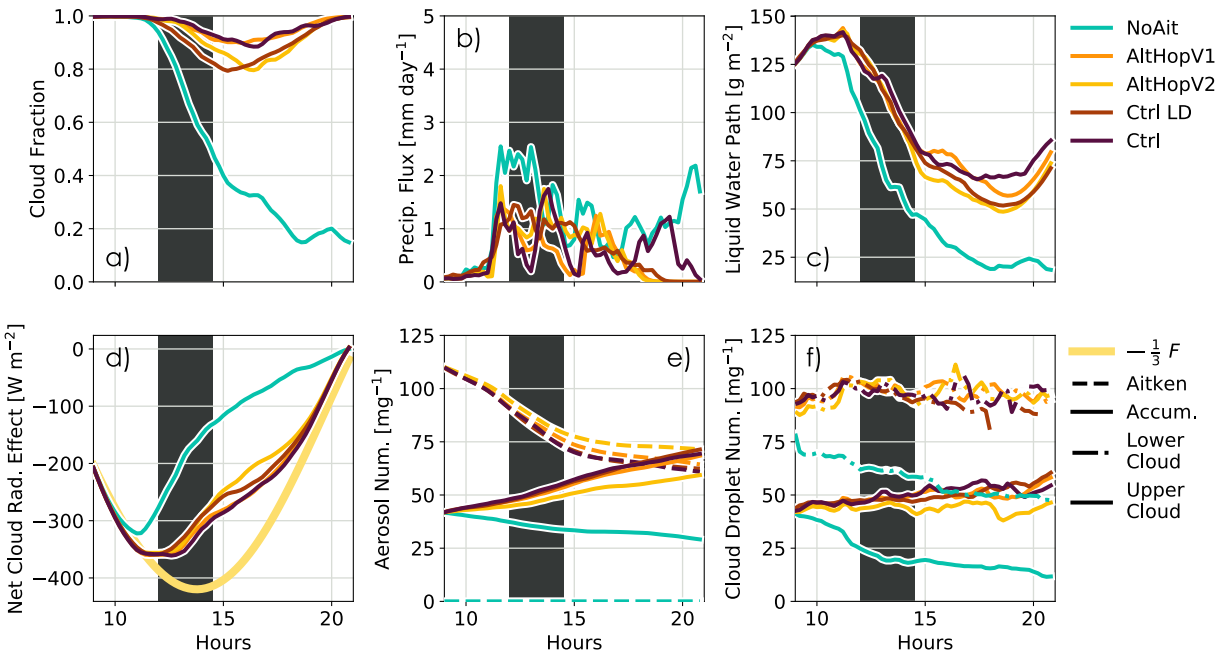

Figure A1. As in Figure 10 but for *Ctrl* and *NoAit* with the *Ctrl LD*, *AltHopV1*, and *AltHopV2* sensitivity studies.

minimum in the cloud layers (Figure S10b, S10d, S10f in Supporting Information S1) and, to a lesser degree, in the less cloudy levels (Figures S10a, S10c, and S10e in Supporting Information S1).

The influence from the transfer slow down from the *Ctrl* to *AltHopV1* to *AltHopV2* is also evident. Like *Ctrl LD*, *AltHopV2* experiences more cloud breakup (Figure A1a), persistent precipitation (b), depletion of LWP (c), and loss of NetCRE (d) than *AltHopV1* and *Ctrl*. Unlike *Ctrl LD*, *AltHopV2* and, to a lesser degree, *AltHopV1* differ in their number concentrations. *AltHopV2* has less Aitken transfer than *AltHopV1*, which, in turn, has slightly less than *Ctrl*. This eventually leads to a noticeable loss of accumulation aerosols and reduces the Sc layer N_d. The effective slow down of Aitken transfer is particularly apparent in the evolution from 10:00 to 14:00 UTC where accumulation number, N_d (Figure S11 in Supporting Information S1), and LWP (Figure S12 in Supporting Information S1) PDFs and statistics shift to smaller values with time for *AltHopV1* and, even more so, for *AltHopV2*. A brief increase in precipitation at 12:00 UTC (Figure S11e in Supporting Information S1) and a slight decrease in τ and NetCRE magnitude by 14:00 UTC (Figure S12h and S12i in Supporting Information S1) suggests slower Aitken buffering in *AltHopV1* and *AltHopV2* compared to the *Ctrl*, which eventually catches up and limits precipitation afterward (Figure A1b).

The difference between *Ctrl* and *NoAit* is substantially larger than any of the variations in the *Ctrl* simulation from the Hoppel Transfer variants or domain size. We thus conclude that the influence of the Aitken aerosols, and particularly the absence of their activation, is a much larger signal than from any variations in the simulation setup that were examined here. These results support the robustness of our conclusions regarding Aitken Buffering and its importance in mid-latitude cloud systems.

Data Availability Statement

All the ACE-ENA campaign observations (J. Wang et al., 2022) used in this study are available at the ARM Climate Research Facility archive at https://www.arm.gov/research/campaigns/aaf2017ace-ena. ECMWF ERA5 Reanalysis profiles developed for the campaign (Tao & Xie, 2011) were used in our study as were the NASA SATCORPS VISST products for ARM (ARM Data Center, 2017). The SAM model (Khairoutdinov & Randall, 2003) is publicly available at http://rossby.msrc.sunysb.edu/SAM.html. Simulation output, forcings, and source code (including the aerosol-enabled microphysics scheme) used in this study are all archived at Zenodo (McCoy, Blossey, et al., 2023).

Acknowledgments
We thank all those who gathered, worked with, and provided data from the ACE-ENA field campaign and the accompanying satellite retrievals. Data were obtained from the Atmospheric Radiation Measurement (ARM) Program sponsored by the U.S. Department of Energy, Office of Science, Office of Biological and Environmental Research, Climate and Environmental Sciences Division. We acknowledge support from the U. S. Department of Energy Atmospheric System Research (DOE ASR) through grants DE-SC0020134 and DE-SC0021103. Research by ILM was supported by the NOAA Climate and Global Change Postdoctoral Fellowship Program, administered by UCAR's Cooperative Programs for the Advancement of Earth System Science (CPAESS) under award NA18NWS4620043B and by the NOAA cooperative agreements NA17OAR4320101 and NA22OAR4320151. CSB acknowledges support from the Allen Institute for AI. This work used Bridges-2 (Brown et al., 2021) at Pittsburgh Supercomputing Center through allocation EES210037 from the Advanced Cyberinfrastructure Coordination Ecosystem: Services & Support (ACCESS) program (Boerner et al., 2023), which is supported by National Science Foundation Grants 2138259, 2138286, 2138307, 2137603, and 2138296, and also through allocation TG-EES210037 as part of the Extreme Science and Engineering Discovery Environment (XSEDE) (Towns et al., 2014), which is supported by NSF ACI-1548562. We thank our editor, Yun Qian; two anonymous reviewers; and Graham Feingold for their suggestions for improving our manuscript. ILM thanks Amy, Daniel, John, and Laura for their insights and support. Finally, we thank Marat Khairoutdinov for developing, maintaining, and sharing SAM.

References

Abdul-Razzak, H., & Ghan, S. J. (2000). A parameterization of aerosol activation: 2. Multiple aerosol types. *Journal of Geophysical Research*, *105*(D5), 6837–6844. https://doi.org/10.1029/1999jd901161

Ackerman, A. S., Kirkpatrick, M. P., Stevens, D. E., & Toon, O. B. (2004). The impact of humidity above stratiform clouds on indirect aerosol climate forcing. *Nature*, *432*(7020), 1014–1017. https://doi.org/10.1038/nature03174

Albrecht, B., Ghate, V., Mohrmann, J., Wood, R., Zuidema, P., Bretherton, C., et al. (2019). Cloud System Evolution in the Trades (CSET): Following the evolution of boundary layer cloud systems with the NSF/NCAR GV. *Bulletin of the American Meteorological Society*, *100*(1), 93–121. https://doi.org/10.1175/BAMS-D-17-0180.1

Albrecht, B. A. (1989). Aerosols, cloud microphysics, and fractional cloudiness. *Science*, *245*(4923), 1227–1230. https://doi.org/10.1126/science.245.4923.1227

ARM Data Center. (2017). Minnis Cloud Products Using Visst Algorithm (VISSTPX2DM10MINNIS) [Dataset]. *Atmospheric Radiation Measurement (ARM) user facility, Eastern North Atlantic (ENA) External Data (satellites and others)*, *11*. Retrieved from https://www.arm.gov/capabilities/science-data-products/vaps/visst/xds

Bellouin, N., Quaas, J., Gryspeerdt, E., Kinne, S., Stier, P., Watson-Parris, D., et al. (2020). Bounding global aerosol radiative forcing of climate change. *Reviews of Geophysics*, *58*(1), e2019RG000660. https://doi.org/10.1029/2019RG000660

Berner, A. H., Bretherton, C. S., Wood, R., & Muhlbauer, A. (2013). Marine boundary layer cloud regimes and POC formation in a CRM coupled to a bulk aerosol scheme. *Atmospheric Chemistry and Physics*, *13*(24), 12549–12572. https://doi.org/10.5194/acp-13-12549-2013

Binkowski, F. S., & Shankar, U. (1995). The Regional Particulate Matter Model: 1. Model description and preliminary results. *Journal of Geophysical Research*, *100*(D12), 26191–26209. https://doi.org/10.1029/95JD02093

Blossey, P. N., Bretherton, C. S., & Mohrmann, J. (2021). Simulating observed cloud transitions in the northeast Pacific during CSET. *Monthly Weather Review*. https://doi.org/10.1175/MWR-D-20-0328.1

Boerner, T. J., Deems, S., Furlani, T. R., Knuth, S. L., & Towns, J. (2023). ACCESS: Advancing Innovation: NSF's Advanced Cyberinfrastructure Coordination Ecosystem: Services & Support. In *Practice and Experience in Advanced Research Computing (PEARC23), July 23–27, 2023, Portland, OR, USA* (p. 4). ACM. https://doi.org/10.1145/3569951.3597559

Boucher, O., Randall, D., Artaxo, P., Bretherton, C., Feingold, G., Forster, P., et al. (2013). Clouds and aerosols. In T. F. Stocker, D. Qin, G.-K. Plattner, M. Tignor, S. K. Allen, J. Doschung, et al. (Eds.), *Climate change 2013: The physical science basis. Contribution of working group I to the fifth assessment report of the Intergovernmental Panel on Climate Change* (pp. 571–657). Cambridge University Press. https://doi.org/10.1017/CBO9781107415324.016

Bretherton, C. S., & Blossey, P. N. (2017). Understanding mesoscale aggregation of shallow cumulus convection using large-eddy simulation. *Journal of Advances in Modeling Earth Systems*, *9*(8), 2798–2821. https://doi.org/10.1002/2017ms000981

Bretherton, C. S., Blossey, P. N., & Uchida, J. (2007). Cloud droplet sedimentation, entrainment efficiency, and subtropical stratocumulus albedo. *Geophysical Research Letters*, *34*(3), L03813. https://doi.org/10.1029/2006gl027648

Brown, S. T., Buitrago, P., Hanna, E., Sanielevici, S., Scibek, R., & Nystrom, N. A. (2021). Bridges-2: A platform for rapidly-evolving and data intensive research. In *Practice and Experience in Advanced Research Computing* (pp. 1–4). https://doi.org/10.1145/3437359.3465593

Bulatovic, I., Igel, A. L., Leck, C., Heintzenberg, J., Riipinen, I., & Ekman, A. M. L. (2021). The importance of Aitken mode aerosol particles for cloud sustenance in the summertime high Arctic – A simulation study supported by observational data. *Atmospheric Chemistry and Physics*, *21*(5), 3871–3897. https://doi.org/10.5194/acp-21-3871-2021

Carslaw, K. S., Lee, L. A., Reddington, C. L., Pringle, K. J., Rap, A., Forster, P. M., et al. (2013). Large contribution of natural aerosols to uncertainty in indirect forcing. *Nature*, *503*(7474), 67–71. https://doi.org/10.1038/nature12674

Christensen, M. W., Gettelman, A., Cermak, J., Dagan, G., Diamond, M., Douglas, A., et al. (2022). Opportunistic experiments to constrain aerosol effective radiative forcing. *Atmospheric Chemistry and Physics*, *22*(1), 641–674. https://doi.org/10.5194/acp-22-641-2022

Clarke, A. D., Varner, J. L., Eisele, F., Mauldin, R. L., Tanner, D., & Litchy, M. (1998). Particle production in the remote marine atmosphere: Cloud outflow and subsidence during ACE 1. *Journal of Geophysical Research*, *103*(D13), 16397–16409. https://doi.org/10.1029/97jd02987

Covert, D. S., Kapustin, V. N., Bates, T. S., & Quinn, P. K. (1996). Physical properties of marine boundary layer aerosol particles of the mid-Pacific in relation to sources and meteorological transport. *Journal of Geophysical Research*, *101*(D3), 6919–6930. https://doi.org/10.1029/95jd03068

Fan, J., Rosenfeld, D., Zhang, Y., Giangrande, S. E., Li, Z., Machado, L. A. T., et al. (2018). Substantial convection and precipitation enhancements by ultrafineaerosol particles. *Science*, *359*(6374), 411–418. https://doi.org/10.1126/science.aan8461

Feingold, G., & Kreidenweis, S. M. (2002). Cloud processing of aerosol as modeled by a large eddy simulation with coupled microphysics and aqueous chemistry. *Journal of Geophysical Research*, *107*(D23). AAC 6–1–AAC 6–15. https://doi.org/10.1029/2002JD002054

Feingold, G., Kreidenweis, S. M., Stevens, B., & Cotton, W. R. (1996). Numerical simulations of stratocumulus processing of cloud condensation nuclei through collision-coalescence. *Journal of Geophysical Research*, *101*(D16), 21391–21402. https://doi.org/10.1029/96JD01552

Gong, X., Wang, Y., Xie, H., Zhang, J., Lu, Z., Wood, R., et al. (2023). Maximum supersaturation in the marine boundary layer clouds over the North Atlantic. *AGU Advances*, *4*(6), e2022AV000855. https://doi.org/10.1029/2022AV000855

Gordon, H., Kirkby, J., Baltensperger, U., Bianchi, F., Breitenlechner, M., Curtius, J., et al. (2017). Causes and importance of new particle formation in the present-day and preindustrial atmospheres. *Journal of Geophysical Research: Atmospheres*, *122*(16), 8739–8760. https://doi.org/10.1002/2017jd026844

Gordon, H., Sengupta, K., Rap, A., Duplissy, J., Frege, C., Williamson, C., et al. (2016). Reduced anthropogenic aerosol radiative forcing caused by biogenic new particle formation. *Proceedings of the National Academy of Sciences*, *113*(43), 12053–12058. https://doi.org/10.1073/pnas.1602360113

Heintzenberg, J., Covert, D. C., & Van Dingenen, R. (2000). Size distribution and chemical composition of marine aerosols: A compilation and review. *Tellus B*, *52*(4), 1104–1122. https://doi.org/10.1034/j.1600-0889.2000.00136.x

Hoffmann, F., & Feingold, G. (2023). A note on aerosol processing by droplet collision-coalescence. *Geophysical Research Letters*, *50*(11), e2023GL103716. https://doi.org/10.1029/2023GL103716

Igel, A. L., Ekman, A. M. L., Leck, C., Tjernström, M., Savre, J., & Sedlar, J. (2017). The free troposphere as a potential source of arctic boundary layer aerosol particles. *Geophysical Research Letters*, *44*(13), 7053–7060. https://doi.org/10.1002/2017GL073808

Ivanova, I. T., & Leighton, H. G. (2008a). Aerosol–cloud interactions in a mesoscale model. Part I: Sensitivity to activation and collision–coalescence. *Journal of the Atmospheric Sciences*, *65*(2), 289–308. https://doi.org/10.1175/2007JAS2207.1

Ivanova, I. T., & Leighton, H. G. (2008b). Aerosol–cloud interactions in a mesoscale model. Part II: Sensitivity to aqueous-phase chemistry. *Journal of the Atmospheric Sciences*, *65*(2), 309–330. https://doi.org/10.1175/2007JAS2276.1

Kaufman, Y. J., & Tanré, D. (1994). Effect of variations in super-saturation on the formation of cloud condensation nuclei. *Nature*, *369*(6475), 45–48. https://doi.org/10.1038/369045a0

Kazil, J., Wang, H., Feingold, G., Clarke, A. D., Snider, J. R., & Bandy, A. R. (2011). Modeling chemical and aerosol processes in the transition from closed to open cells during VOCALS-REx. *Atmospheric Chemistry and Physics*, *11*(15), 7491–7514. https://doi.org/10.5194/acp-11-7491-2011

Khairoutdinov, M. F., & Randall, D. A. (2003). Cloud Resolving modeling of the ARM summer 1997 IOP: Model formulation, results, uncertainties, and sensitivities. *Journal of the Atmospheric Sciences*, *60*(4), 607–625. https://doi.org/10.1175/1520-0469(2003)060<0607:CRMOTA>2.0.CO;2

Konsta, D., Dufresne, J., Chepfer, H., Vial, J., Koshiro, T., Kawai, H., et al. (2022). Low-level marine tropical clouds in six CMIP6 models are too few, too bright but also too compact and too homogeneous. *Geophysical Research Letters*, *49*(11), e2021GL097593. https://doi.org/10.1029/2021GL097593

Lawler, M. J., Saltzman, E. S., Karlsson, L., Zieger, P., Salter, M., Baccarini, A., et al. (2021). New insights into the composition and origins of ultrafine aerosol in the summertime high Arctic. *Geophysical Research Letters*, *48*(21), e2021GL094395. https://doi.org/10.1029/2021GL094395

Leahy, L. V., Wood, R., Charlson, R. J., Hostetler, C. A., Rogers, R. R., Vaughan, M. A., & Winker, D. M. (2012). On the nature and extent of optically thin marine low clouds. *Journal of Geophysical Research*, *117*(D22), D22201. https://doi.org/10.1029/2012JD017929

McCoy, I. L., Blossey, P. N., Wyant, M. C., Bretherton, C. S., & Wood, R. (2023). Supporting data for the manuscript: "Aitken-mode aerosols buffer decoupled mid-latitude boundary layer clouds against precipitation depletion" [Software and Dataset]. *Zenodo, 0.1*. https://doi.org/10.5281/zenodo.8088443

McCoy, I. L., Bretherton, C. S., Wood, R., Twohy, C. H., Gettelman, A., Bardeen, C. G., & Toohey, D. W. (2021). Influences of recent particle formation on Southern Ocean aerosol variability and low cloud properties. *Journal of Geophysical Research-Atmospheres*, *126*(8), e2020JD033529. https://doi.org/10.1029/2020JD033529

McCoy, I. L., McCoy, D. T., Wood, R., Regayre, L., Watson-Parris, D., Grosvenor, D. P., et al. (2020). The hemispheric contrast in cloud microphysical properties constrains aerosol forcing. *Proceedings of the National Academy of Sciences*, *117*(32), 18998–19006. https://doi.org/10.1073/pnas.1922502117

McCoy, I. L., McCoy, D. T., Wood, R., Zuidema, P., & Bender, F. A. (2023). The role of mesoscale cloud morphology in the shortwave cloud feedback. *Geophysical Research Letters*, *50*(2), e2022GL101042. https://doi.org/10.1029/2022GL101042

Mieslinger, T., Stevens, B., Kölling, T., Brath, M., Wirth, M., & Buehler, S. A. (2021). Optically thin clouds in the trades. *Atmospheric Chemistry and Physics Discussions*, *2021*, 1–33. https://doi.org/10.5194/acp-2021-453

Minnis, P., Nguyen, L., Palikonda, R., Heck, P. W., Spangenberg, D. A., Doelling, D. R., et al. (2008). Near-real time cloud retrievals from operational and research meteorological satellites. In R. H. Picard, A. Comeron, K. Schäfer, A. Amodeo, & M. V. Weele (Eds.), *Remote Sensing of Clouds and the Atmosphere XIII* (Vol. 7107). SPIE. (Backup Publisher: International Society for Optics and Photonics). https://doi.org/10.1117/12.800344.710703

Minnis, P., Smith, W. L., Jr., Young, D. F., Nguyen, L., Rapp, A. D., Heck, P. W., et al. (2001). A near-real time method for deriving cloud and radiation properties from satellites for weather and climate studies. In *Proceedings of AMS 11th Conference Satellite Meteorology and Oceanography, Madison, WI (October 15–18)* (pp. 477–480).

Minnis, P., Sun-Mack, S., Young, D. F., Heck, P. W., Garber, D. P., Chen, Y., et al. (2011). CERES edition-2 cloud property retrievals using TRMM VIRS and Terra and Aqua MODIS data—Part I: Algorithms. *IEEE Transactions on Geoscience and Remote Sensing*, *49*(11), 4374–4400. https://doi.org/10.1109/TGRS.2011.2144601

Mlawer, E. J., Taubman, S. J., Brown, P. D., Iacono, M. J., & Clough, S. A. (1997). Radiative transfer for inhomogeneous atmospheres: RRTM, a validated correlated-k model for the longwave. *Journal of Geophysical Research*, *102*(D14), 16663–16682. https://doi.org/10.1029/97JD00237

Mohrmann, J., Bretherton, C. S., McCoy, I. L., McGibbon, J., Wood, R., Ghate, V., et al. (2019). Lagrangian evolution of the Northeast Pacific marine boundary layer structure and cloud during CSET. *Monthly Weather Review*, *147*(12), 4681–4700. https://doi.org/10.1175/mwr-d-19-0053.1

Morrison, H., Curry, J. A., & Khvorostyanov, V. I. (2005). A new double-moment microphysics parameterization for application in cloud and climate models. Part I: Description. *Journal of the Atmospheric Sciences*, *62*(6), 1665–1677. https://doi.org/10.1175/JAS3446.1

Narenpitak, P., Kazil, J., Yamaguchi, T., Quinn, P., & Feingold, G. (2021). From sugar to flowers: A transition of shallow cumulus organization during ATOMIC. *Journal of Advances in Modeling Earth Systems*, *13*(10), e2021MS002619. https://doi.org/10.1029/2021ms002619

Neggers, R. A. J., Chylik, J., Egerer, U., Griesche, H., Schemann, V., Seifert, P., et al. (2019). Local and remote controls on arctic mixed-layer evolution. *Journal of Advances in Modeling Earth Systems*, *11*(7), 2214–2237. https://doi.org/10.1029/2019MS001671

O, K.-T., Wood, R., & Bretherton, C. S. (2018). Ultraclean layers and optically thin clouds in the stratocumulus-to-cumulus transition. Part II: Depletion of cloud droplets and cloud condensation nuclei through collision–coalescence. *Journal of the Atmospheric Sciences*, *75*(5), 1653–1673. https://doi.org/10.1175/jas-d-17-0218.1

O, K.-T., Wood, R., & Tseng, H.-H. (2018). Deeper, precipitating PBLs associated with optically thin veil clouds in the Sc-Cu transition. *Geophysical Research Letters*, *45*(10), 5177–5184. https://doi.org/10.1029/2018gl077084

Pöhlker, M. L., Zhang, M., Campos Braga, R., Krüger, O. O., Pöschl, U., & Ervens, B. (2021). Aitken mode particles as CCN in aerosol- and updraft-sensitive regimes of cloud droplet formation. *Atmospheric Chemistry and Physics*, *21*(15), 11723–11740. https://doi.org/10.5194/acp-21-11723-2021

Price, R., Baccarini, A., Schmale, J., Zieger, P., Brooks, I. M., Field, P., & Carslaw, K. S. (2023). Late summer transition from a free-tropospheric to boundary layer source of Aitken mode aerosol in the high Arctic. *Atmospheric Chemistry and Physics*, *23*(5), 2927–2961. https://doi.org/10.5194/acp-23-2927-2023

Rogers, R. R., & Yau, M. K. (1989). *A short course in cloud physics* (3rd ed.). Elsevier, Butterworth-Heinemann. ISBN: 978-0-7506-3215-7

Sanchez, K. J., Chen, C. L., Russell, L. M., Betha, R., Liu, J., Price, D. J., et al. (2018). Substantial seasonal contribution of observed biogenic sulfate particles to cloud condensation nuclei. *Scientific Reports*, *8*(1), 3235. https://doi.org/10.1038/s41598-018-21590-9

Sanchez, K. J., Roberts, G. C., Saliba, G., Russell, L. M., Twohy, C., Reeves, M. J., et al. (2021). Measurement report: Cloud processes and the transport of biological emissions affect southern ocean particle and cloud condensation nuclei concentrations. *Atmospheric Chemistry and Physics*, *21*(5), 3427–3446. https://doi.org/10.5194/acp-21-3427-2021

Seinfeld, J. H., & Pandis, S. N. (2016). *Atmospheric chemistry and physics: From air pollution to climate change* (3rd ed.). John Wiley & Sons, Incorporated. ISBN: 978-1-118-94740-1

Sterzinger, L. J., & Igel, A. L. (2024). Above-cloud concentrations of cloud condensation nuclei help to sustain some Arctic low-level clouds. *Atmospheric Chemistry and Physics*, *24*(6), 3529–3540. https://doi.org/10.5194/acp-24-3529-2024

Stevens, B., & Feingold, G. (2009). Untangling aerosol effects on clouds and precipitation in a buffered system. *Nature*, *461*(7264), 607–613. https://doi.org/10.1038/nature08281

Tao, C., & Xie, S. (2011). 3-hourly VARANAL for ACE-ENA June 2017 to February 2018 [Dataset]. https://doi.org/10.5439/1602289

Tornow, F., Ackerman, A. S., Fridlind, A. M., Cairns, B., Crosbie, E. C., Kirschler, S., et al. (2022). Dilution of boundary layer cloud condensation nucleus concentrations by free tropospheric entrainment during marine cold air outbreaks. *Geophysical Research Letters*, *49*(11), e2022GL098444. https://doi.org/10.1029/2022GL098444

Towns, J., Cockerill, T., Dahan, M., Foster, I., Gaither, K., Grimshaw, A., et al. (2014). XSEDE: Accelerating scientific discovery. *Computing in Science & Engineering*, *16*(5), 62–74. https://doi.org/10.1109/MCSE.2014.80

Twohy, C. H., Clement, C. F., Gandrud, B. W., Weinheimer, A. J., Campos, T. L., Baumgardner, D., et al. (2002). Deep convection as a source of new particles in the midlatitude upper troposphere. *Journal of Geophysical Research*, *107*(D21). AAC 6–1–AAC 6–10. https://doi.org/10.1029/2001jd000323

Twomey, S. (1959). The nuclei of natural cloud formation part I: The chemical diffusion method and its application to atmospheric nuclei. *Geofisica Pura e Applicata*, *43*(1), 227–242. https://doi.org/10.1007/BF01993559

Twomey, S. (1977). The influence of pollution on the shortwave albedo of clouds. *Journal of the Atmospheric Sciences*, *34*(7), 1149–1152. https://doi.org/10.1175/1520-0469(1977)034<1149:TIOPOT>2.0.CO;2

Wang, J., Pikridas, M., Spielman, S. R., & Pinterich, T. (2017). A fast integrated mobility spectrometer for rapid measurement of sub-micrometer aerosol size distribution, Part I: Design and model evaluation. *Journal of Aerosol Science*, *108*, 44–55. https://doi.org/10.1016/j.jaerosci.2017.02.012

Wang, J., Wood, R., Jensen, M. P., Chiu, J. C., Liu, Y., Lamer, K., et al. (2022). Aerosol and Cloud Experiments in the Eastern North Atlantic (ACE-ENA). *Bulletin of the American Meteorological Society*, *103*(2), E619–E641. https://doi.org/10.1175/bams-d-19-0220.1

Wang, S., Wang, Q., & Feingold, G. (2003). Turbulence, condensation, and liquid water transport in numerically simulated nonprecipitating stratocumulus clouds. *Journal of the Atmospheric Sciences*, *60*(2), 262–278. https://doi.org/10.1175/1520-0469(2003)060<0262:TCALWT>2.0.CO;2

Williamson, C. J., Kupc, A., Axisa, D., Bilsback, K. R., Bui, T., Campuzano-Jost, P., et al. (2019). A large source of cloud condensation nuclei from new particle formation in the tropics. *Nature*, *574*(7778), 399–403. https://doi.org/10.1038/s41586-019-1638-9

Wood, R. (2006). Rate of loss of cloud droplets by coalescence in warm clouds. *Journal of Geophysical Research*, *111*(D21), D21205. https://doi.org/10.1029/2006jd007553

Wood, R. (2012). Stratocumulus clouds. *Monthly Weather Review*, *140*(8), 2373–2423. https://doi.org/10.1175/mwr-d-11-00121.1

Wood, R., O, K.-T., Bretherton, C. S., Mohrmann, J., Albrecht, B. A., Zuidema, P., et al. (2018). Ultraclean layers and optically thin clouds in the stratocumulus-to-cumulus transition. Part I: Observations. *Journal of the Atmospheric Sciences*, *75*(5), 1631–1652. https://doi.org/10.1175/jas-d-17-0213.1

Wyant, M. C., Bretherton, C. S., & Blossey, P. N. (2018). The sensitivity of numerical simulations of cloud-topped boundary layers to cross-grid flow. *Journal of Advances in Modeling Earth Systems*, *10*(2), 466–480. https://doi.org/10.1002/2017ms001241

Wyant, M. C., Bretherton, C. S., Wood, R., Blossey, P. N., & McCoy, I. L. (2022). High free-tropospheric Aitken-mode aerosol concentrations buffer cloud droplet concentrations in large-eddy simulations of precipitating stratocumulus. *Journal of Advances in Modeling Earth Systems*, *14*(6), e2021MS002930. https://doi.org/10.1029/2021MS002930

Xu, W., Ovadnevaite, J., Fossum, K. N., Lin, C., Huang, R.-J., Ceburnis, D., & O'Dowd, C. (2022). Sea spray as an obscured source for marine cloud nuclei. *Nature Geoscience*, *15*(4), 282–286. https://doi.org/10.1038/s41561-022-00917-2

Xue, H., & Feingold, G. (2006). Large-eddy simulations of trade wind cumuli: Investigation of aerosol indirect effects. *Journal of the Atmospheric Sciences*, *63*(6), 1605–1622. https://doi.org/10.1175/JAS3706.1

Zender, C. (2001). Particle size distributions: Theory and application to aerosols, clouds, and soils.

Zheng, G., Kuang, C., Uin, J., Watson, T., & Wang, J. (2020). Large contribution of organics to condensational growth and formation of cloud condensation nuclei (CCN) in the remote marine boundary layer. *Atmospheric Chemistry and Physics*, *20*(21), 12515–12525. https://doi.org/10.5194/acp-20-12515-2020

Zheng, G., Wang, Y., Aiken, A. C., Gallo, F., Jensen, M. P., Kollias, P., et al. (2018). Marine boundary layer aerosol in the eastern North Atlantic: Seasonal variations and key controlling processes. *Atmospheric Chemistry and Physics*, *18*(23), 17615–17635. https://doi.org/10.5194/acp-18-17615-2018

Zheng, G., Wang, Y., Wood, R., Jensen, M. P., Kuang, C., McCoy, I. L., et al. (2021). New particle formation in the remote marine boundary layer. *Nature Communications*, *12*(1), 527. https://doi.org/10.1038/s41467-020-20773-1